

LABORATORY REPORT

PART II

Rock Mechanical Investigations
on Rock Salt Samples recovered from the Zuid-
wending Cavern Site

—Test Results and Parameter Evaluation —



INSTITUT FÜR
GEBIRGSMECHANIK
GMBH



INSTITUT FÜR
GEBIRGSMECHANIK
GMBH

Rock Mechanical Investigations
on Rock Salt Samples recovered from the Zuidwending Cavern Site

— Test Results and Parameter Evaluation —

Customer/client: Nobian
Boortorenweg 27
7554 RD Hengelo
The Netherlands

Purchase Order No. (client): 4501392578 and 4501409408

Order No. (contractor): B_IfG_56/2022 and B_IfG_27/2023

Authors:
Dr. Johannes Herrmann
Dipl.-Geol. Dirk Naumann
Dipl.-Geol. Christopher Rölke

Leipzig, April 11, 2024

A handwritten signature in blue ink, appearing to read "Ralf-Michael Günther".

Dr.-Ing. Ralf-Michael Günther
Managing Director

A handwritten signature in blue ink, appearing to read "Dirk Naumann".

Dipl.-Geol. Dirk Naumann
Head of Geomechanical Laboratory

CONTENT

1	INTRODUCTION AND OBJECTIVES.....	1
2	SAMPLE MATERIAL AND ROCK MECHANICAL TEST PROGRAM.....	3
2.1	Sample Material.....	3
2.2	Experimental Setup and Technique	8
2.2.1	<i>Pre-Tests</i>	8
2.2.2	<i>Long-term creep tests</i>	10
2.2.3	<i>Permeability Experiments</i>	12
3	RESULTS	16
3.1	Pre-Tests	16
3.2	Long – term constant stress (creep) tests	20
3.3	Permeability experiments	25
4	SUMMARY.....	30
	REFERENCES.....	32
	APPENDIX	33
A1:	Specimens – Pre-Tests I-I	34
A2:	Specimens – Pre-Tests I-II	35
A3:	Specimens – Pre-Tests II	36
A4:	Pre-Tests – Experimental protocol and stress-strain behavior.....	37
A5:	Specimens - creep experiments I-I	40
A6:	Specimens – creep experiments I-II	41
A7:	Specimens - creep experiments II-I	42
A8:	Specimens - creep experiments II-II	43
A9:	Specimens - creep experiments III	44
A10:	Recorded creep curves during deformation	45
A11:	Samples prepared for hydraulic conductivity testing.....	56
A12:	Recorded creep curves and flow paths during hydraulic conductivity testing	58

1 INTRODUCTION AND OBJECTIVES

Nobian assigned the *Institut für Gebirgsmechanik GmbH (IfG Leipzig)* to perform a suite of laboratory rock mechanical testing on specimens prepared from rock salt material recovered during a drilling campaign performed in the 1960's at the the Zuidwending Cavern Site located in The Netherlands. The drilled cores have been stored at the Dutch Geological Service (TNO). The overall content and procedure of the planned project is very similar to a previously finished project, which was carried out to determine the specific rock mechanical as well as hydraulic properties of rock salt material recovered from a borehole drilled into the Heiligerlee Cavern site (Herrmann et al., 2023). Therefore, parts of the described materials, apparatuses and achieved results are also applicable for this project.

To assure the integrity and a safe operation of the cavern, a sound geo-mechanical as well as micro-structural understanding of the host rock is mandatory. Therefore, deducing rock physical and hydraulic parameters in addition to long-term creep properties and their relation to microstructural features is essential; especially with respect to performing research on long-term abandonment and its integrated processes, such as grain size dependent pressure solution creep. To this end, an extensive rock mechanical and hydraulic as well as microstructural testing program has been developed by *Nobian*, *IfG Leipzig* and the *Microstructures and Pores GmbH (MaP)*. The latter acts as an additional project partner, which is responsible for the microstructural analyses due to their extensive expertise on this field. Special note is given to the late Prof. Janos Urai who initially setup the idea of re-crystallizing the sample to reduce the grain size and be able to measure pressure solution creep.

With respect to the rock mechanical and hydraulic testing program conducted in the laboratories of *IfG Leipzig*, the following protocol has been agreed upon:

(1) Sample preparation and characterization

- a. Preparation of cylindrical specimens at varying dimensions (length, diameter) to fit given apparatus geometrical requirements.
- b. Petrophysical characterization of the sample material; including ultrasonic wave velocity, density, and water content.
- c. Photographic documentation of the prepared specimen prior to and after testing.
- d. Preparation of salt material in terms of powder of each sample before testing for geochemical analyses, which will be done by *MaP* in their laboratories.

(2) Rock mechanical and hydraulic testing

- a. To run long-term creep tests at (in situ) representative conditions, *Nobian* and *IfG Leipzig* agreed upon the performance of Pre-Tests to characterize the general response to mechanical loading of the sample material. These Pre-Tests are represented by triaxial constant strain rate tests conducted at constant confining pressure at elevated temperatures, where the (partly brine-saturated) samples are deformed up to an axial strain of ~ 20%. Afterwards, the samples will be wrapped and sent to *MaP* for detailed microstructural investigations.
- b. Based on the lessons learned from the Pre-Tests, long-term creep experiments will be performed at elevated confining pressure and temperature, including a re-saturation of the samples to a state of natural brine content. The initial loading conditions were chosen to be relatively high to accomplish pronounced initial strain values and followed changing stress levels, which was expressed by progressively decreasing differential stress levels.
- c. Conducting triaxial hydraulic conductivity experiments and a temperature of 40°C and brine as flow medium at increasing fluid pressures to determine the permeability of the rock material.
- d. Preparation of additional specimens (including sample characterization as described in (1a-d), which will be experimented at constant stress (creep) conditions in an underground research laboratory in the Altaussee Mine (AT) and geochemically analyzed (powder material) by *MaP*. Before shipping, the prepared samples will have been Pre-Tested by *IfG Leipzig* at either the same conditions as described in (a) or isostatic loading conditions with no noteworthy sample deformation in axial direction.

2 SAMPLE MATERIAL AND ROCK MECHANICAL TEST PROGRAM

According to the desired parameters to determine as well as the overall constitution of the rock material (drill cores) a suitable sample preparation and experimental testing protocol was chosen.

2.1 Sample Material

The test material is solely represented by rock salt cores (see Figure 1) recovered from a depth of 243 – 1796 m (Table 1) of the Zuidwending borehole drilled close to the Zuidwending village (NL), which is almost entirely placed in the first cycle of the Permian Zechstein-lithology (Z1) (Strohmenger et al., 1996).

Prior to shipping to IfG Leipzig a careful selection of suitable core material for testing was made by MaP to ensure that representative sample material is investigated. To prevent (negative) weathering effects due to elevated relative humidity, the chosen core segments have been wrapped in plastic foil. Additionally, sufficient cushioning was provided to prevent mechanical damage of the sample material upon shipping.



Figure 1: Core samples (selected) of the Zuidwending well drilled close to the Zuidwending village as received at IfG Leipzig.

In general, the received sample material displayed a halite matrix of medium (mm-scale) to large sized grains (cm-scale) with some additional anhydrite features (Figure 1). The former is mostly oriented as sub-parallel bedding somewhat dipping at a low angle at medium grain size, whereas the latter is either diffusely accumulated or in a few cases appears as substantial layer within the surrounding matrix. This becomes apparent by the usage of transmitting light as has been done as part of the characterization

of the prepared specimens for testing (Figure 2). The received sample material was dried in an oven for 24 hours at a temperature of $T = 105\text{ }^{\circ}\text{C}$. The water content of the sample material was afterwards calculated by taking the ratio of evaporated water over sample mass, yielding a low average water content of $w_T = 0.02\text{ }\%$. Note: This value is close to the resolution/uncertainty of the used scale ($\Delta m = \pm 0.02\text{ g}$, see below). However, it allows to qualify the investigated rocks as low water content material.

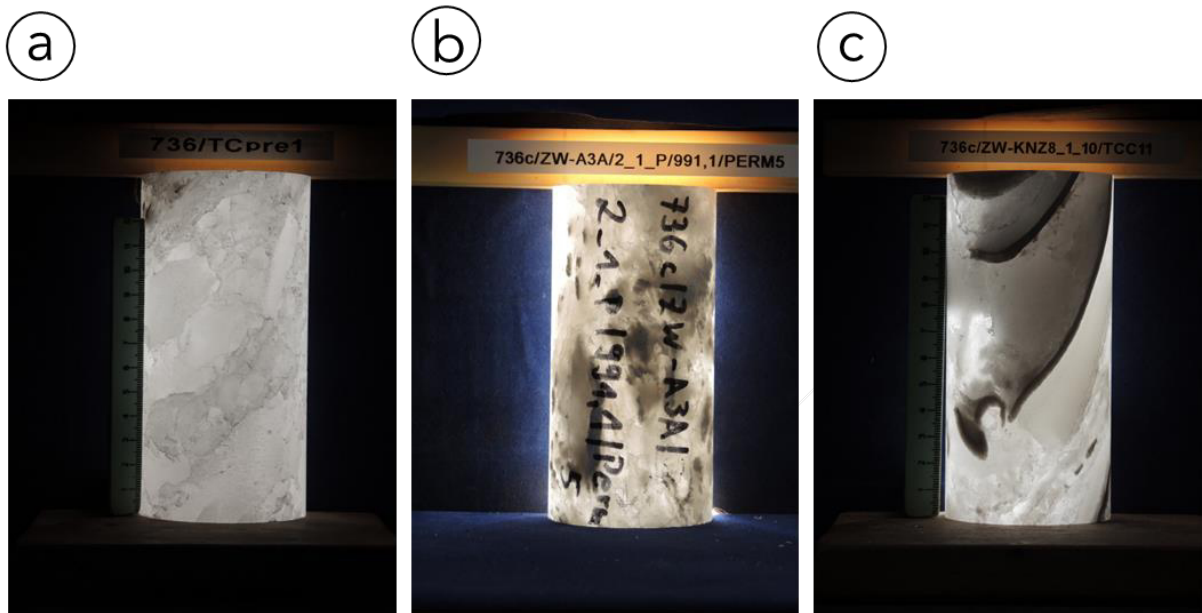


Figure 2: Varying sample mineralogy and orientation made visible by the usage of transmitting light. (a) and shows the medium to coarse-grained halite matrix. Anhydrite is accumulated either randomly (b) or in layers within the halite matrix (c).

All experiments were performed on cylindrical specimens including plan-parallel end-surfaces (e.g., Figure 2) prepared by using a rock cutting saw and a lathe to ensure high accuracy regarding sample dimensions and alignment (edges plane parallel to each other and normal to the central axis). Given the fact that three main types of rock mechanical and hydraulic tests were performed, different requirements regarding the sample dimensions needed to be met depending on the used deformation apparatus (Table 1). After preparation, the specimens were carefully handled and sealed to prevent external influences such as sample disturbance and relative humidity reducing the geometric quality of the samples. Prior to testing, sample dimensions and weight were measured to calculate their bulk density at an accuracy of length and mass fluctuations of $\Delta l = \pm 0.02\text{ mm}$ and $\Delta m = \pm 0.02\text{ g}$, respectively. The density of the specimens used for mechanical and hydraulic testing was determined to range from $\rho = 2.103 - 2.236\text{ g/cm}^3$, resulting in an average value of $\rho_{av} = 2.180\text{ g/cm}^3$ with a standard deviation of $\Delta\rho = 0.028\text{ g/cm}^3$ (Table 1). Assuming densities of $\rho_{\text{Anhydrite}} = 2.964\text{ g/cm}^3$ and $\rho_{\text{Halite}} = 2.163\text{ g/cm}^3$

for Anhydrite and Halite, respectively, one may use Equation 1 to estimate an average anhydrite content of 3 wt% of the investigated samples:

$$\frac{1}{\rho_{av}} = \frac{wt\%_{Anhydrite}}{\rho_{Anhydrite}} + \frac{1-wt\%_{Anhydrite}}{\rho_{Halite}} \quad (1)$$

Prior to testing, samples have been stored at climate-controlled conditions ($T \approx 35^{\circ}\text{C}$, $H_r < 30\%$) due to their fragile nature with respect to relative humidity. Further characterization of the samples was done in terms of ultrasonic pulse measurements (P- and S-Waves) to identify material integrity as well as homogeneity and (an)isotropy characteristics in addition to derive dynamic elastic parameters (e.g., Young's modulus, Poisson's ratio etc.). However, some specimens exhibited internal micro fractures, which did not allow the waves to pass through the sample and therefore no ultrasonic velocities could be calculated in these cases (Table 1):

Table 1: Overview on sample dimensions including petrophysical properties of the specimens.

Specimen No.	Well	Core depth [m]	Experiment	Length [mm]	Diameter [mm]	Density (ρ) [g/cm ³]	f_{Anh} [wt%]	E_{dyn} [GPa]	v_{dyn}
736/TCPre1	A2A	1467.80	Pre-Test, IfG	140.16	70.14	2.161	0	/	/
736/TCPre2	A1A	1506.90	Pre-Test, IfG	140.26	70.17	2.170	1	/	/
736/TCPre3	KNZ	1795.70	Pre-Test, IfG	140.12	70.08	2.175	2	/	/
736/TCPre4	A1A	1518.30	Pre-Test, IfG	140.36	70.22	2.165	0	33.25	0.29
736/TCPre5	KNZ	1627.80	Pre-Test, IfG	140.20	70.14	2.150	0	/	/
736c/TC2	A7B	1401.18	Pre-Test, Altaussee	140.11	70.33	2.190	5	/	/
736c/TC3	A7B	1401.38	Pre-Test, Altaussee	140.17	70.28	2.191	5	/	/
736c/TC4	A7B	1401.58	Pre-Test, Altaussee	140.22	70.25	2.181	3	/	/
736c/TC5	A2A	1505.90	Pre-Test, Altaussee	140.05	70.28	2.159	0	/	/
736/ZW/TCC1	A1A	453.00	Creep	130.22	63.14	2.166	1	35.36	0.28
736/ZW/TCC2	A1A	959.50	Creep	130.16	63.11	2.160	0	35.52	0.25
736/ZW/TCC3	KNZ	1627.60	Creep	130.21	63.14	2.211	8	29.44	0.32
736/ZW/TCC4	A3A	991.30	Creep	130.19	63.11	2.230	11	38.60	0.25
736/ZW/TCC5	A4A	1028.50	Creep	130.23	63.17	2.195	5	38.28	0.24
736/ZW/TCC6	A8A	543.00	Creep	130.21	63.15	2.168	1	36.72	0.24
736/ZW/TCC7	A2B	651.40	Creep	130.16	63.31	2.159	0	33.31	0.27
736/ZW/TCC8	A3A	592.40	Creep	130.28	63.25	2.214	9	22.00	0.40
736/ZW/TCC9	A3A	1445.30	Creep	130.19	63.31	2.103	0	34.61	0.27
736/ZW/TCC10	A7B	1469.50	Creep	130.20	63.31	2.156	0	32.49	0.30
736/ZW/TCC11	KNZ	243.30	Creep	130.17	63.29	2.212	8	30.58	0.33

736/ZW/TCC12	A5A	1190.90	Creep	130.25	63.29	2.170	1	27.14	0.36
736/ZW/Perm1	A1A	1518.10	Permeability	120.06	59.66	2.181	3	37.49	0.23
736/ZW/Perm2	A1A	453.20	Permeability	120.09	59.73	2.175	2	37.14	0.25
736/ZW/Perm3	A2A	1506.10	Permeability	120.11	59.56	2.179	3	34.41	0.28
736/ZW/Perm4	A3A	592.20	Permeability	120.20	63.06	2.201	6	33.47	0.32
736/ZW/Perm5	A3A	991.10	Permeability	120.18	59.61	2.236	12	34.31	0.30
736/ZW/Perm6	A3A	1445.10	Permeability	120.10	63.04	2.200	6	29.45	0.33

f_{Anh} = fraction of Anhydrite within the sample, E_{dyn} = (dynamic) Young's modulus, v_{dyn} = (dynamic) Poisson's ratio. **Note:** Some specimens did not allow to measure p/s-wave velocities most likely due to internal integrities (micro cracks), which did not allow the wave to pass through the samples.

2.2 Experimental Setup and Technique

The experimental protocols used to perform the planned experiments are generally in line with the "Standard Testing Methods formulated by ASTM" as well as the "ISRM suggested methods" (ASTM International, 1996, 1998, 2001, 2002, 2004, 2005, 2016; Ulusay & Hudson, 2015). However, minor adaptions (e.g., jacket material, storage capacities, preparation protocol) to fit the IfG – test procedures that have been developed may have been applied.

Three different main types of experiments (1) Pre-Tests, (2) creep, and (3) permeability, have been performed, which required individual sample dimensions. Therefore, the experimental setup and used technique will be described separately for each experiment type in the following.

2.2.1 Pre-Tests

Three Pre-Tests were performed on cylindrical specimens ($l \times d \approx 140 \times 70$ mm) utilizing a servo-hydraulic triaxial press (D2000 GL Testsystems or RBA 2500 Schenck//Trebel, and MTS-TestStar-software; see Figure 3), which allowed to generate the necessary stress in axial ($\sigma_{\text{axial}} = \sigma_1$) as well as lateral direction ($\sigma_3 = p_c$). The cylindrical samples were sealed with rubber jackets or shrinking tubes to prevent the confining medium (oil) from intruding into the pores of the specimens. To capture sample deformation in axial direction, three LVDT transducers are mounted outside of the pressure vessel between the piston and the loading frame. The axial load is recorded by an externally mounted load cell ($F_{\text{max}}=2500$ kN, $\Delta F = \pm 0.1681$ kN). The Pre-tests were conducted at elevated temperatures ($T=90 - 100^\circ\text{C}$) to advance occurring deformation mechanisms.

Throughout the entire testing program, the following parameters were measured automatically: axial displacement (Δl), axial load (F), confining pressure ($p_c=\sigma_3$) and lateral deformation ΔC . After the triaxial tests have been performed, the sample volume changes ΔV were calculated from axial and lateral deformation. The volume change of the sample corresponds to the dilatancy parameter or compaction in case of volume loss.

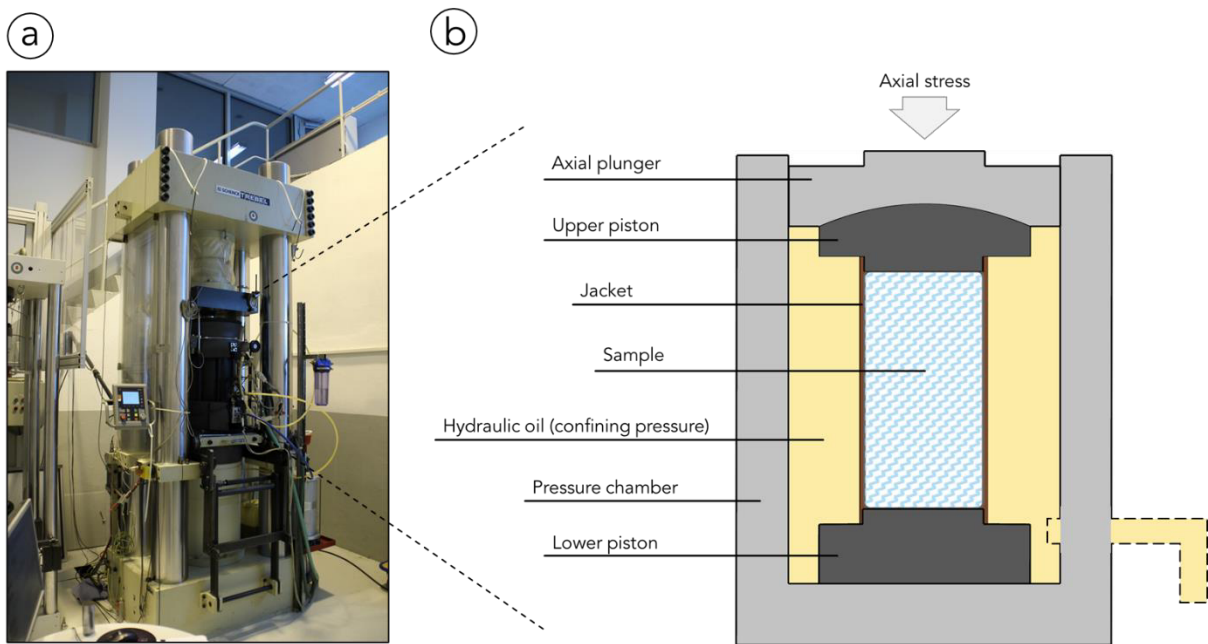


Figure 3: Servo-hydraulic triaxial press (here: RBA 2500 Scheck/Trebel/) used to run Pre-Tests: loading frame with installed pressure vessel (a), including a sketch of the used pressure vessel (b).

The conversion of the measured values to differential stress and strains is given by:

$$\sigma_{diff} = (\sigma_1 - \sigma_3) * (1 - \varepsilon_1) = \left(\frac{F}{A_0} - \sigma_3 \right) * (1 - \varepsilon_1) \quad (2)$$

$$\varepsilon_1 = \frac{\Delta l}{l_0} \quad (3)$$

$$\varepsilon_3 = \frac{\Delta C}{C_0} \quad (4)$$

$$\varepsilon_{Vol} = \varepsilon_1 + 2 * \varepsilon_3 \quad (5)$$

(Equation 5 assumes a bi-axial deformation, $\varepsilon_2 = \varepsilon_3$, ignoring cross-terms as they are minor.)

where:

$\sigma_{diff}, \sigma_1, \sigma_3$ axial differential stress, axial stress, lateral stress = confining pressure (p_d)

$\varepsilon_1, \varepsilon_3$ axial strain, lateral strain (both engineering strain)

F axial load

A_0 initial cross-sectional area

$l_0, \Delta l$ initial sample length, axial sample displacement

$C_0, \Delta C$ initial sample circumference, current sample circumference

The triaxial loading frame (incl. the pressure control system) is installed in a climate-controlled laboratory (temperature ranging by $\Delta T = \pm 2^\circ\text{C}$). To ensure constant volume within the loading system before

changing the applied confining pressure, a dwelling period of at least one hour was kept guaranteeing stable experimental conditions.

The goal of conducting the Pre-Tests was to generally characterize the mechanical response to different loading schemes of the sample material, which is expressed by its stress – strain behavior. Therefore, the performed Pre-Tests were run at two separate stages:

1st stage: Reconsolidation – isotropic state – Due to recovering procedures after core drilling (stress relaxation) and the long storage period, the core material exhibits dilatancy features, such as unloading cracks. Thus, prior to axial loading, samples were first consolidated in a hydrostatic loading cycle ($\sigma_1 = \sigma_3$) at the desired stress level of $\sigma_1 = \sigma_3 = 20$ MPa.

2nd stage: Triaxial test cycle – deviatoric stage – After increasing the temperature to the desired value ($T = 100$ °C), the samples were loaded at constant strain rates of $\dot{\epsilon} = 1 \times 10^{-5}$ or $1 \times 10^{-6}\text{s}^{-1}$ until the pre-defined maximum axial strain (ϵ_1) was reached ($\epsilon_1 \approx 20\%$) to induce microstructural changes within the sample material. Note, that these experiments were run very carefully to ensure that the samples did not exhibit failure. However, one sample did show some indication of failure (details are given in Paragraph 3.1). To generate data at representative/ in situ conditions, brine ($\pm 0.6\text{ml} \leq 0.1\text{ vol\%}$ of the specimen) was added between the rubber jacket and the sample.

In addition to the mentioned Pre-Test performed to gain knowledge useful for further testing in our laboratories, we also performed four additional Tests at $T = 90$ °C, which were afterwards sent to the Underground Research Laboratory in Altaußsee for further investigations. These focus on creep tests at low deviatoric stresses (Bérest et al., 2019). Three of these samples were loaded (quasi) isostatically for 70—80-hours at $\sigma_1 = \sigma_3 = 20.5 \pm 0.5$ MPa. The remaining sample was deformed following the same protocol as described above.

2.2.2 Long-term creep tests

In total, 12 creep experiments have been performed at elevated constant confining pressure and temperature using cylindrical samples (diameter \times length = $\sim 63\text{ mm} \times 130\text{ mm}$), which were covered by rubber jackets to prevent the confining medium (hydraulic oil) from intruding into the sample. Additionally, low amounts of brine ($V_{\text{Brine}} = 0.5\text{ ml}$) were added to six samples (~TCC7 – TCC12); between the lateral surface of the specimen and the jacket. Samples ~TCC1 – TCC6 have been deformed without additional brine due to an oversight. However, this allowed to quantify a possible effect of free brine (which was not evident). Hydraulic apparatuses equipped with a triaxial cell have been utilized to

conduct the constant axial stress creep tests (Figure 4). After the specimen was installed into the triaxial creep test cell, the confining pressure (p_c) with an accuracy of 1 % of the absolute value was applied. Axial stresses were applied by a hydraulic storage-system connected to an accumulator to provide constant pressures (Figure 4). The utilized apparatuses allow to apply axial forces (F) and confining pressures of up to $F = 247$ kN (translating into axial stresses of 79 MPa) and $p_c = 30$ MPa, respectively. Temperatures of up to $T = 120$ °C are feasible to be applied. Prior to testing, the axial load exerted onto the sample was calibrated for each apparatus/ experiment individually. A dial gauge is mounted at the center on the top plate of the triaxial cell to record sample displacement at a resolution of ± 0.001 mm.

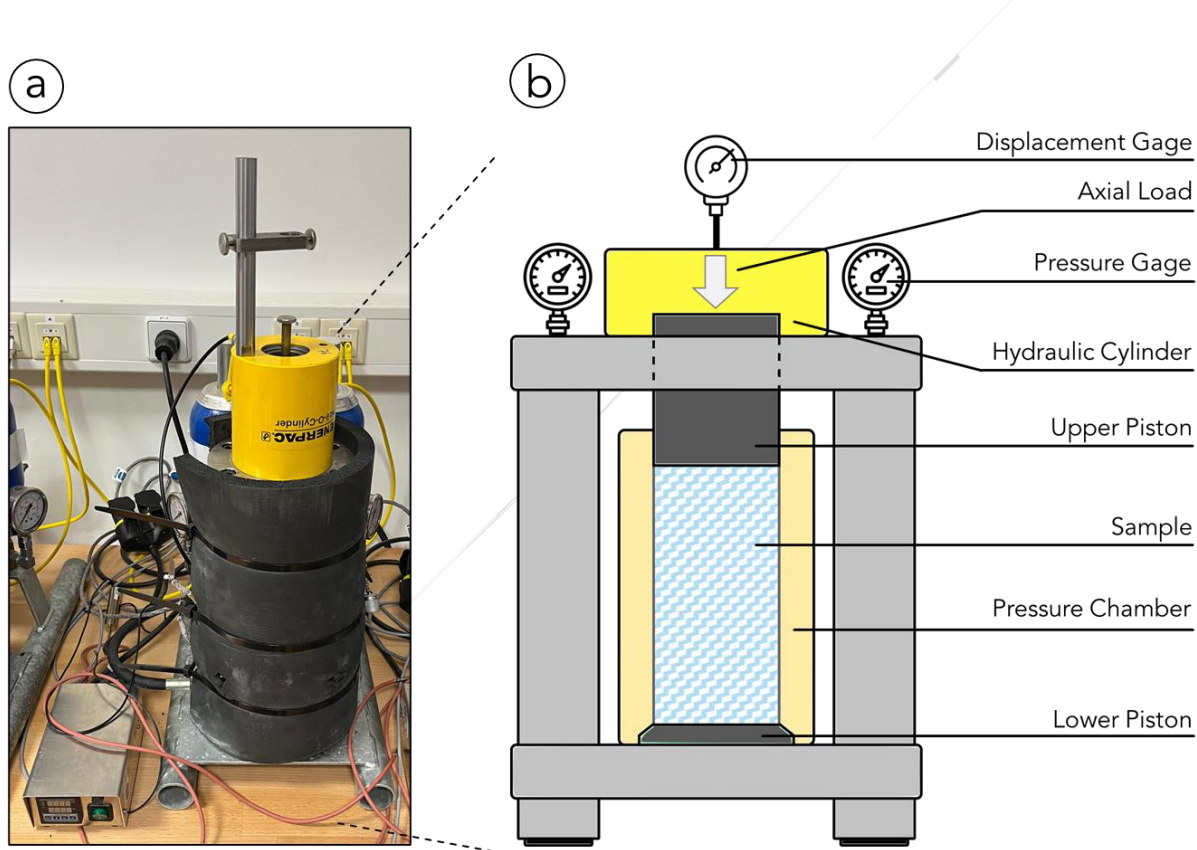


Figure 4: Hydraulic (creep) apparatus equipped with a triaxial cell (a) and a technical drawing of the used setup (b).

To ensure the accuracy of the recorded creep data, a correction to account for frictional phenomena between the moveable piston and O-rings used for sealing has been applied. Possible effects on the recorded displacements induced by variations in room temperature are negligible. A detailed description regarding the correction for frictional effects as well as negligible temperature effects are given in Herrmann et al., 2023.

All experiments conducted to unravel the creep properties of the investigated rock salt material have been performed at elevated confining pressures ($p_c = 12 - 18 \text{ MPa}$) and at controlled constant temperature ($T = 100 \pm 1^\circ\text{C}$). For six experiments, a confining pressure of $p_c = 12 \text{ MPa}$ was chosen to enable a higher differential stress in the first load step (with the pre-tests being performed beforehand to guarantee that no dilatancy occurs during creep deformation). Additionally, constant axial stresses of $\sigma_1 = 15 - 40 \text{ MPa}$, resulting in axial differential stresses of $\sigma_{\text{diff}} \leq 38 \text{ MPa}$ have been applied to induce a long-term time-dependent creep deformation of the sample. The latter has been applied after the samples have been subjected to isostatic stress conditions of $\sigma_1 = \sigma_3 = 18$ and 12 MPa , respectively, during a consolidation phase of three days to prevent the influence of possible unloading features upon core recovery on the creep properties of the sample material. Testing duration of all experiments was 130 ± 1 days (plus three days consolidation phase), with this period starting from the first measurement after the differential stress was exerted onto the specimen. To ensure a constant axial stress level throughout the entity of each experiment, the axial load was increased according to the lateral sample deformation under the assumption of a constant sample volume:

$$A_{\varepsilon_1} = \frac{A_0}{(1-\varepsilon_1)} \quad (6)$$

where A_{ε_1} = cross-sectional at a given axial strain.

Additionally, the apparatus' stiffness is being taken into account with respect to calculated strain values based on recorded displacement measurements.

2.2.3 Permeability Experiments

A total number of six experiments were performed to characterize the hydraulic properties of the investigated sample material. To ensure representative boundary conditions, the tests were performed at elevated confining and fluid pressure, axial stress as well as temperature. Additionally, brine was chosen as flow medium to avoid possible solution processes during the flow period in addition to enable pressure solution creep and sample healing.

The tests were conducted by using hydraulic creep apparatuses comparable to the ones used to run creep experiments (see Figure 4), equipped with a triaxial cell, which was modified to fit an external pore pressure system. The fluid injection pressure (of the brine) was realized by either using a Quizix® syringe pump system or manifold system that allows to run two experiments in parallel. Figure 5 shows

a schematic sketch of the used loading frame with the Quizix® pore pressure system connected to the internal pressure chamber. The application as well as the maximum absolute number and accuracy of axial and radial stresses (confining pressure) in addition to temperature ($T = 40^\circ\text{C}$) is analogue to the description of the performed creep tests (see paragraph 2.2.2).

Cylindrical samples with dimensions of diameter \times length $\approx 60 \text{ mm} \times 120 \text{ mm}$ were covered by a rubber jacket to prevent the hydraulic oil (used to apply the desired confining pressure) from intruding into the sample.

All experiments were conducted by incorporating a radial flow regime (see colorful arrows in Figure 5 indicating the flow direction) of the saturated brine used as flow medium. This was done to avoid a possible circumferential flow between the lateral surface of the specimen and the rubber jacket, which is likely to appear at fluid injection pressures close to the confining pressure, if an axial flow regime would have been chosen. Therefore, a small injection chamber sealed from the rest of the sample was prepared at a desired place within the specimen. The brine is being injected into this chamber which forces a flow in radial direction through the sample (see Figure 5). Additionally, a small reservoir of powdered salt material is being placed on the top of every sample, which the brine passes before entering the injection chamber. The purpose of this reservoir is to compensate possible saturation changes due to temperature differences, which may lead to solution processes inside the sample. To capture the exiting brine volume at the lateral surface of the sample, a mesh made of metal was placed according to the position of the injection chamber. The mesh is connected to a sintered metal plate, which ultimately allows to collect and direct the brine volume into a burette to measure its absolute value. Note: The (outflow) pressure in the burette was throughout the entire testing protocol kept constant at $p_{\text{out}} = 0.1 \text{ MPa}$.

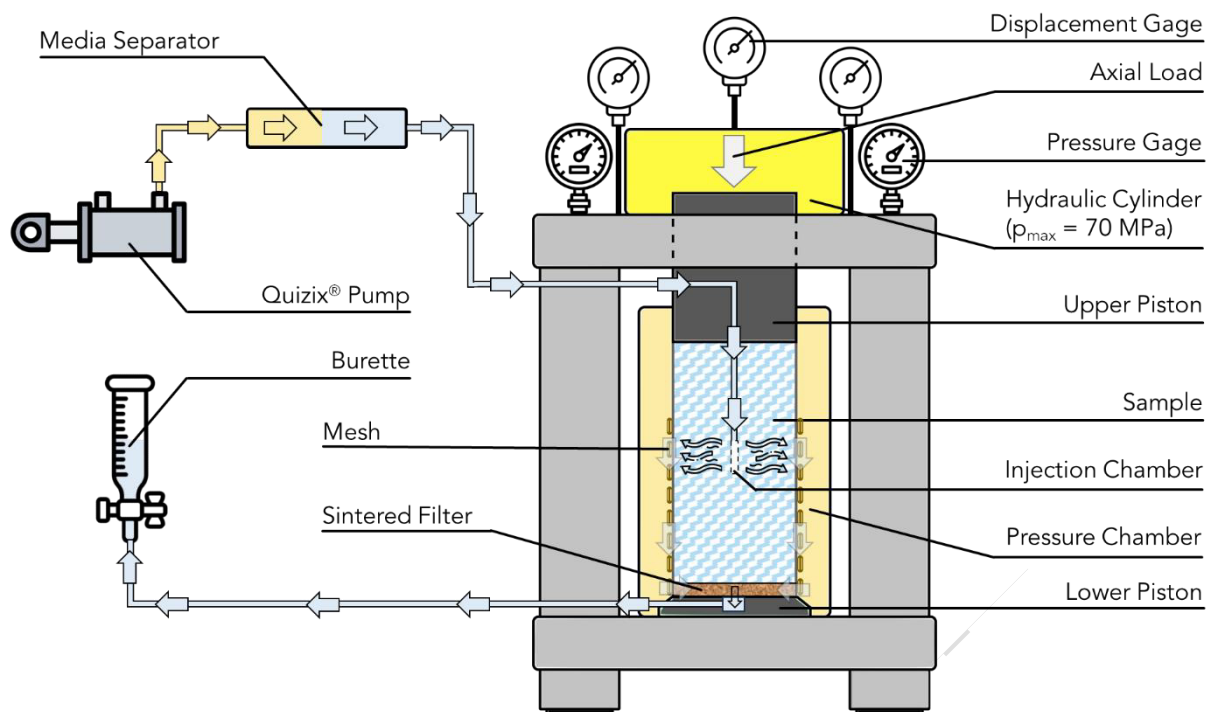


Figure 5: Technical drawing of the used setup to perform conductivity experiments at elevated confining and pore pressure as well as temperature. Arrows indicate the flow direction of the brine used as flow medium (light blue color).

Due to its corrosive properties, the brine was not directly carried by the pump system. Instead, a media separator with a hydraulic oil – brine interface was used. The accuracy of the injection volume and pressure is in the order of 0.001 ml, 0.01 bar (Quizix®) and 0.05 ml, 1.0 bar (Manifold), respectively. The conducted tests followed a complex protocol for every individual experiment and becomes evident by observing at the plotted data accordingly. In general, the injection pressure is increased at a pre-defined ramp after the confining pressure and temperature reached the desired level.

The measured data (confining pressure, axial load, temperature, injection pressure, injection rate, in-flow volume, out-flow volume) is plotted in real time to be able to react to occurrences of any sort and make necessary adjustments after talking to the project partners. After the detection of a breakthrough of the brine through the sample, which is expected at high injection pressures, the injection is stopped, allowing the sample to heal itself (closing of the breakthrough fracture) for a given time.

This is followed by another injection period. Bear in mind, that not all samples displayed time-dependent healing due to its heterogeneous and anisotropic nature.

Neither does such a loading scheme represent stationary conditions nor does it guarantee laminar flow, which are both prerequisites to calculate rock permeabilities following Darcy's law (Atangana, 2018). Additionally, a single-phase flow as well as no reaction between the brine and the sample (induced by thermal gradients) cannot be guaranteed. Therefore, no absolute permeability values are given here, but the precisely measured data including relative changes, which can be used for further analysis.



3 RESULTS

Given the different nature of the performed experiments, results obtained from the rock mechanical as well as hydraulic testing are described separately for each individual type of experiment.

3.1 Pre-Tests

To acquire a basic understanding regarding the general response of the investigated rock material towards mechanical loading, a series of short-term constant strain rate (Pre-) tests has been performed at elevated confining pressures and temperatures (see Table 1). To gain further insight into the defining mechanisms, it was envisioned to ship the deformed, but still intact specimens (as well as powder material prepared from the same core segments) to the *Microstructures and Pores GmbH (MaP)* for detailed microstructural and geochemical examination. To this end, a total number of five Pre-Tests were performed.

The specimens are defined by relatively large grain Halite material with minor additional minerals (Figure 6, Figure A1, A3). Before the samples were covered in jackets and installed into the deformation apparatus, brine ($V_{\text{Brine}} = 0.6 \text{ ml}$) was placed on the end- as well as lateral surface.

The experimental protocol (Figure 7, Figure A4) as example for all Pre-Tests is described in the following:

1. Application of (quasi) isostatic loading conditions ($p_c = 20 \text{ MPa}$)
2. Increasing the temperature to $T = 100 \text{ }^\circ\text{C}$
3. Application of axial differential stress by deforming the sample at a constant axial strain rate of either $\dot{\epsilon} = 1 \times 10^{-6} \text{s}^{-1}$ or $\dot{\epsilon} = 1 \times 10^{-5} \text{s}^{-1}$.
4. Cooling phase at (quasi) isostatic loading conditions ($p_c = 20 \text{ MPa}$)
5. Unloading phase and disassembly

The main difference between the different experiments is in the applied constant axial strain rate of the deformed specimens. All samples have been deformed up axial strains of $\epsilon_{\text{axial}} \approx 20 \%$ (Figure 7, Figure A4). The recorded maximum axial stresses during deformation ranges between $\sigma_{\text{axial}} = 32 - 50 \text{ MPa}$. A positive correlation between applied axial strain rate and recorded axial stress is observable. All samples except for one (736/ZW/TCPre4) displayed ductile deformation and strain hardening accompanied by progressively slightly decreasing volumetric strain (Figure 7, Figure A4).

Generally, the volumetric strain remained positive throughout the entire experimental duration, indicating a smaller sample volume at the end of the experiment if compared to its initial value. The slightly decreasing volumetric strain value may be induced by a change in deformation direction (axial – radial direction). The recorded deformation curves may suggest that no brittle features such as dilatancy occurred during the deformation. However, to proof such claim, detailed microstructural investigations are mandatory (Rutter, 1986) Specimen 736/ZW/TCPre4, did exhibit some brittle deformation expressed by a slight, abrupt drop in axial stress at an axial strain of $\epsilon_{\text{axial}} \approx 11.66\%$. After disassembly, the deformed sample contained a macroscopic shear fracture. However, it did not fail entirely (Figure A2). The deformation of the other four samples was accommodated by pronounced bulging and barreling of the specimens. Comparing the photographs taken at transmitting light before and after deformation, microstructural changes expressed mostly by grain size reduction and reorientation may be evident (Figure 6, Figure A2). Detailed microstructural analyses were beyond the scope of our laboratory protocol and can therefore be found in the descriptions provided by *Microstructures and Pores GmbH (MaP)*.

The microstructural features of the four samples (pre)deformed to be shipped afterwards to the Underground Research Laboratory in Altaußsee (AT) are similar to the one of the Pre-Test samples. Sample 736/ZW/TC3, displayed the same overall deformation behavior despite being tested at slightly lower temperature ($T = 90\text{ }^{\circ}\text{C}$) with a maximum axial stress of $\sigma_{\text{axial}} = 44\text{ MPa}$ and strain of $\epsilon_{\text{axial}} \approx 20\%$. Deformation was again accommodated by bulging and barreling in addition to grain size reduction (Figure A2). The other three samples, which have been deformed at (quasi)isostatic conditions (Figure 7, Figure A4) and $T = 90\text{ }^{\circ}\text{C}$ have been wrapped and sealed carefully immediately upon disassembly to guarantee intact samples for further testing. Therefore, no photographs showing the deformed specimens are available.

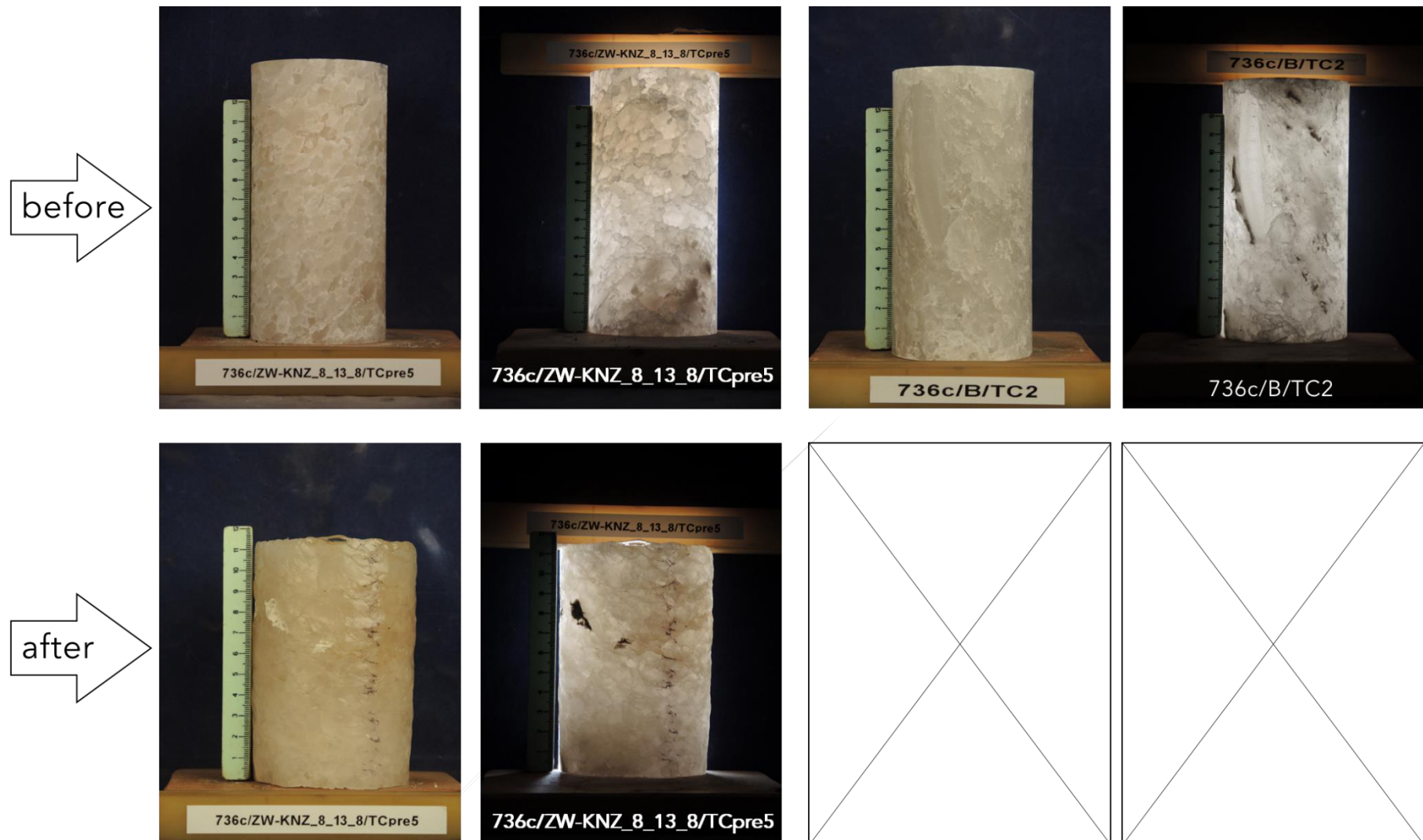


Figure 6: Specimens 736/ZW/TCPre5 and 736/ZW/TC2 before (upper row) and after successful testing (lower row) in the frame of the planned Pre-Tests. Sample 736/ZW/TCPre5 displays deformation accommodated mostly by bulging/barreling accompanied by microstructural changes, which becomes apparent by comparing the photographs taken at transmitted light before and after the experiments were conducted.

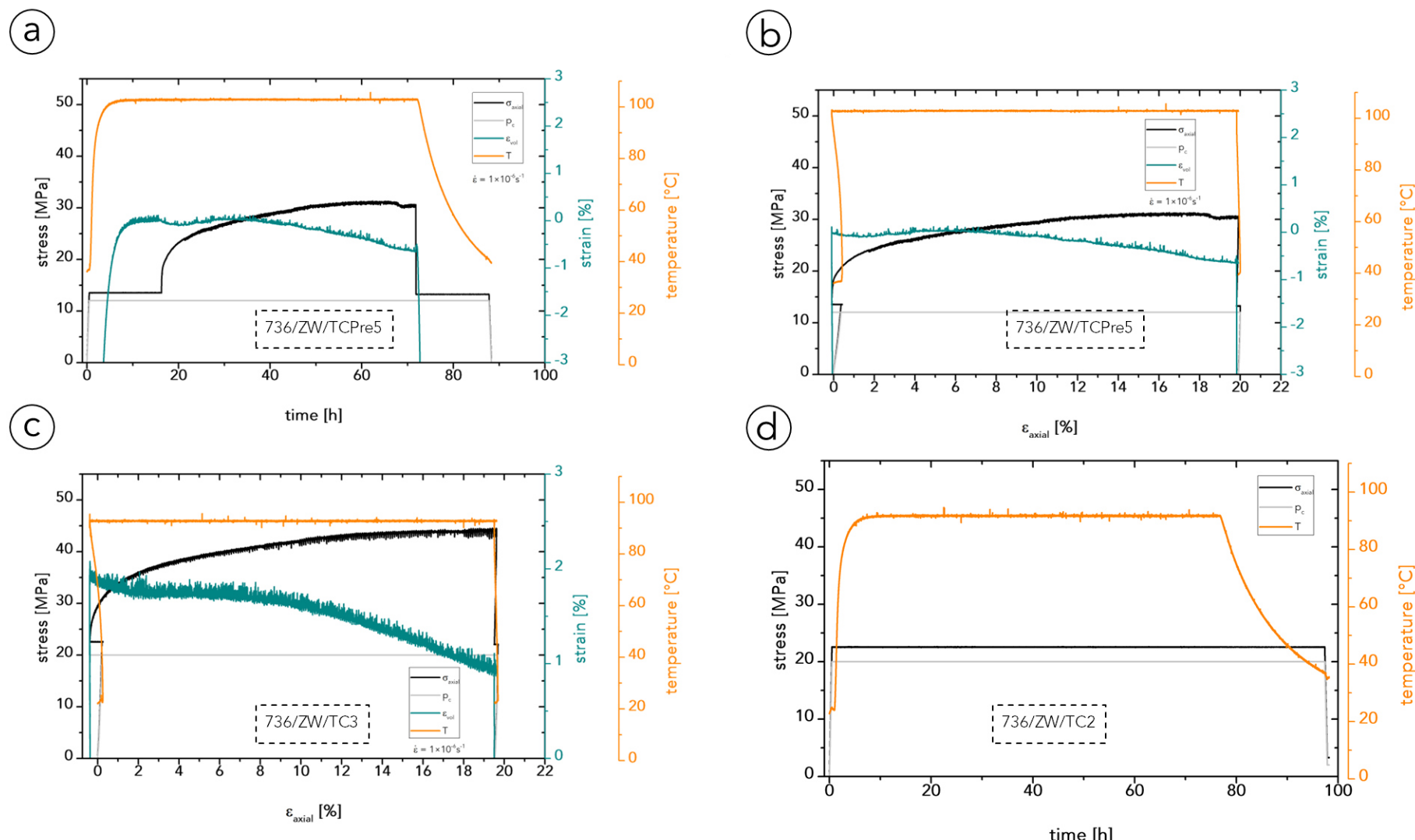


Figure 7: Experimental protocol (a, d) and recorded stress – strain curves (including volumetric strain) of the deformed samples (b, c). Sample descriptions are indicated. Samples in (a, b, c) display ductile deformation behavior.

3.2 Long – term constant stress (creep) tests

In total, 12 creep experiments at elevated confining pressure and a temperature of $T = 100 \pm 2^\circ\text{C}$ were performed. The tests can be divided into two batches: (1) samples 736/ZW/TCC1-TCC6, which have been performed at a confining pressure of $p_c = 18 \text{ MPa}$ and (2) samples 736/ZW/TCC7-TCC12, where the confining pressure was held constant at $p_c = 12 \text{ MPa}$ (Table 1, Table 2).

Table 2: Experimental conditions during long – term constant stress (creep) tests. All experiments have been performed at constant temperate of $T = 100 \pm 2^\circ\text{C}$.

Specimen No.	p_c	σ_{1_I}	σ_{1_II}	σ_{1_III}	σ_{1_IV}	σ_{1_VI}	$\sigma_{\text{diff_min}}$	$\dot{\epsilon}_{\text{diff_min}}$	ϵ_{max}
		[MPa]						[$\times 10^{-11}\text{s}^{-1}$]	[%]
736/ZW/TCC1	18	39,5	28	20	21	/	2	1,64	20,27
736/ZW/TCC2	18	39,5	28	20	21	/	2	1,2	19,97
736/ZW/TCC3	18	39,5	28	20	21	/	2	0,59	19,34
736/ZW/TCC4	18	39,5	28	23	/	/	5	6,34	18,71
736/ZW/TCC5	18	39,5	28	23	22	/	4	6,51	19,01
736/ZW/TCC6	18	39,5	28	23	22	/	4	7,02	20,2
736/ZW/TCC7	12	40	22	17	16	/	4	5,05	20,64
736/ZW/TCC8	12	40	22	17	16	/	4	7,84	20,36
736/ZW/TCC9	12	40	22	17	16	/	4	6,92	20,95
736/ZW/TCC10	12	40	22	17	16	/	4	4,43	19,23
736/ZW/TCC11	12	40	22	17	16	15	3	6,12	23,44
736/ZW/TCC12	12	40	22	17	16	15	3	0,56	20,38

p_c = confining pressure, $\sigma_{1,x}$ = axial stress at the individual loading phase, $\sigma_{\text{diff_min}}$ = minimum axial differential stress, $\dot{\epsilon}_{\text{diff_min}}$ = (quasi) constant strain rate at minimum axial differential stress and ϵ_{max} = final axial strain and the end of the individual experiment.

Samples 736/ZW/TCC7-TCC12 were additionally treated by adding small amounts of brine ($V_{\text{Brine}} = 0.5 \text{ ml}$) between the sample and the jacket prior to installing into the deformation apparatus. In general, two different loading schemes were applied during creep testing: (1) a hydrostatic loading phase of three days, (2) followed by individual loading phases characterized by varying additional axial stresses. The individual loading phase of each experiment is given in Table 2. The loading scheme was designed with the intention to induce large axial strains at a short experimental duration to create substantial microstructural changes; hence the high axial differential stress of the first phase of each loading scheme.

In line with the overall description of the sample material (see paragraph 2.1), the specimens prepared for long – term creep testing are defined by a halite matrix consisting of either medium or large grains ranging from a few millimeters to centimeters (Figure 8, Figure A5-9). Additionally, some specimens also contained some amounts of Anhydrite, which was either diffusely distributed or formed in layers/bands (Figure A5-9). Figure 8 shows the specimen 736/ZW/TCC1 prior to and after testing as example.

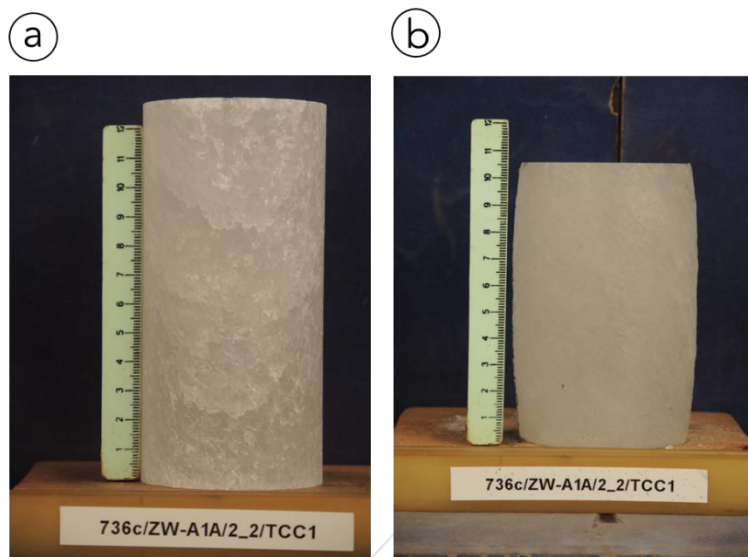


Figure 8: Specimen 736/ZW/TCC1 prior to (a) and after testing (b) at constant axial differential stresses and elevated confining pressure. Temperature was constant at $T = 100^\circ\text{C}$. The specimen displays substantial final axial deformation at a strain of $\epsilon_{\max,\text{TCC1}} = 20.27\%$.

An overview regarding the microstructural features of the remaining samples (prior to and after testing) is given in the appendix (Figure A5-9). All samples exhibit a substantial amount of final axial deformation at the end of the experiment represented by axial strains of $\epsilon_{\max} = 18.71 - 23.44\%$ (Table 2) with the deformation being accommodated by either barreling or bulging of the specimen (Figure 8, Figure A5-9) or in cases of Anhydrite layers crossing the halite matrix by additional shearing along these layers (sample 736/ZW/TCC11 in Figure A8). Here, the formation of macroscopic shearing bands led to a puncture of the jacket. Therefore, the sample was exposed to the oil, which was used as confining medium. The sample has been discarded for further investigations. However, one might argue that due to its low permeability and negligible Biot's coefficient, that the observed deformation behavior is still representative.

For loading scheme (1), following the initial hydrostatic phase, the axial differential stress was chosen to successively decrease to minimum values of $\sigma_{\text{diff_min}} = 2 - 5$ up to the second to last phase. Depending on the individual specimen and its response to the axial load, in some cases the applied load was either further slightly decreased or increased (Table 2, Figure 9, Figure A10a-e). Figure 9a-c provides an overview on the different deformation phases of loading scheme (1). Here, sample 736/ZW/TCC1 was once again chosen as a representative.

After the initial hydrostatic phase, the differential stress throughout loading scheme (2) was consequently decreasing for each individual phase to reach minimum values of $\sigma_{\text{diff_min}} = 4$ and 5 MPa, respectively, in the final phase (see Table 2). The recorded creep curves of the remaining samples are provided in the appendix (Figure A10f-k). Depending on the applied deformation conditions, the samples displayed varying strain rates throughout the experimental duration (Figure 9d). Also, reaching a (quasi) secondary creep phase defined by constant strain rate may be valid only for the deformation phase at minimum axial differential stress. Therefore, we calculated a (quasi) constant strain rate ($\dot{\epsilon}$), expressed by the first derivative of strain over time, only for these phases (Table 2). However, we want to emphasize that the strain rates provided in Table 2 most likely do not represent constant creep rates but estimates (quasi) since longer (experimental) deformation periods at low axial differential stresses are necessary to guarantee a constant deformation rate.

Observing the data given Table 2 individually for the two different loading schemes suggests fluctuating strain rates independent of the minimum axial differential stresses. However, considered both sets of experiments, one may define a weak positive correlation between applied axial differential stress and resulting strain rate. However, we want to emphasize that more data is necessary to proof this assumption. In general, the calculated strain rates are relatively low, ranging from $\dot{\epsilon}_{\sigma_{\text{diff_min}}} = 0.59 - 7.84 \times 10^{-11} \text{ s}^{-1}$. Given the variety of microstructural features of the investigated samples, we don not aim to extrapolate to actual constant strain rate values. However, some literature data may suggest values up to one order of magnitude lower than the presented strain rates of this report (Bérest et al., 2019). Note that the literature values represent creep rates at ambient confining pressure. At elevated confining pressures, calculated creep rates may be even lower.

Independent of the applied loading scheme, all samples exhibit substantial axial strains within the first deviatoric phase. However, inspecting the final strain values of the individual specimens of the two

different loading schemes, it appears that the samples deformed at confining pressures of $p_c = 18$ MPa (loading scheme (1) show generally somewhat lower values than the specimen of the second set (loading scheme (2), $p_c = 12$ MPa, Table 2).



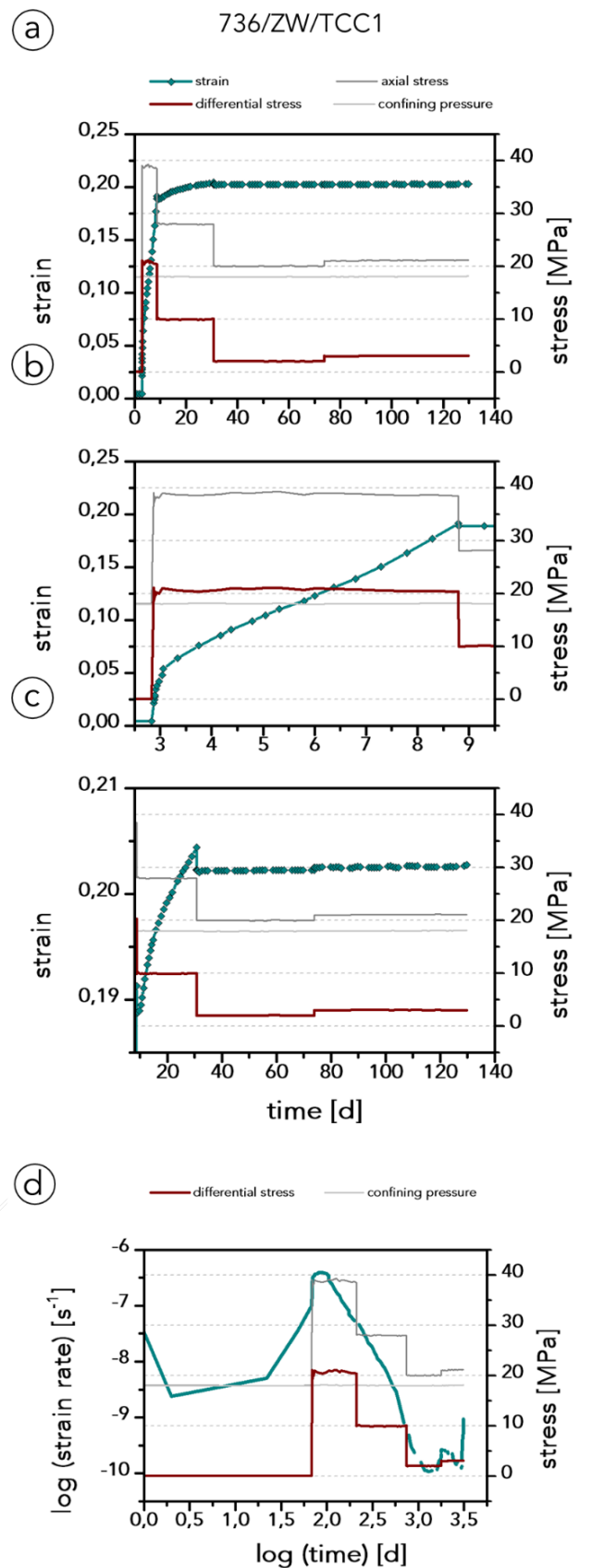


Figure 9: (a) Creep curve of specimen 736/ZW/TCC1 recorded during deformation at varying constant axial differential stress levels resulting from applied axial stresses (σ_1) and confining pressures (p_c). For better clarity, subfigures (b) and (c) show individual experimental phases at higher magnification. (d) shows the calculated strain rate expressed by the first order derivative of axial

strain as function of applied axial differential stress in log-log space. Temperature was constant during the entire experiment at $T = 100 \text{ }^{\circ}\text{C}$.

3.3 Permeability experiments

In total, six experiments were performed to unravel the hydraulic properties of the investigated salt rock material at elevated confining pressures and temperatures as well as constant axial stresses (Table 1, Table 2, Table 3).

In general, the specimens used to quantify the hydraulic properties of the investigated sample material display similar microstructural features, if compared to samples prepared for long-term (creep) deformational testing. These are typically expressed by a halite matrix consisting of either medium or large grains (mm to cm scale) and partly anhydrite inclusions or layers somewhat inclined throughout the sample (Figure 10, Figure A 11). One example is given in Figure 10, showing the specimen 736/ZW/Perm1 before (a) and after testing (b). This sample mostly consists of halite and some minor amounts of anhydrite either randomly distributed or as vein, which becomes evident by observing the picture taken at transmitting light conditions. Here, the injection chamber for the brine was placed mostly in the halitic part.

Photographs taken before and after testing of the remaining samples prepared for conductivity investigations are given in the appendix (Figure A 11) for clarity reasons. The individual structural distinctiveness of each sample becomes evident by studying the photographs taken at transmissive lighting. Also, the influence of structural features on possible pathways for the brine can be taken from these photographs, knowing that the injection chamber is placed central with respect to the sample dimensions.



Figure 10: Specimen 736c/ZW-A1A/9_1_P/1518,05/PERM1 (a) before (at ambient and transmitted lighting conditions) as well as after (b) testing at elevated axial stress and confining pressure to determine conductive properties against brine. Dotted area in (b) displays where the breakthrough of the brine occurred. Temperature was constant at $T = 40^\circ\text{C}$.

Table 3: Overview on experimental protocol for hydraulic conductivity testing

Specimen No.	Test duration [d]	σ_1 [MPa]	p_c [MPa]	Pumped brine volume [ml]	$p_{\text{Brine_BT}}$ [MPa]
736c/ZW/Perm1	47	16	15	333	10.5
736c/ZW/Perm2	50	16//20	15	96	15.2
736c/ZW/Perm3	53	16	15	200	16.4
736c/ZW/Perm4	53	16	15	13	/
736c/ZW/Perm5	53	16	15	30	13.6
736c/ZW/Perm6	52	16	15	31	/

σ_1 = axial stress, p_c = confining pressure and $p_{\text{Brine_BT}}$ = brine injection pressure at breakthrough.

The overarching experimental protocol is similar for every experiment performed. (0) Initially, the temperature in the loading cell was increased to $T = 40^\circ\text{C}$ prior to applying stresses and injection pressures. (1) A hydrostatic loading phase ($\sigma_1 = p_c$) of at least three days was realized at which the injection pressure of the brine did not exceed values of $p_{\text{Brine}} = 2 \text{ MPa}$ to ensure sample integrity. In some cases, the axial differential stress ($\sigma_{\text{diff}} = \sigma_1 - p_c$) was slightly increased to guarantee force fit- and stable deformation conditions at elevated injection pressures at a later experimental stage (Table 1). (2) To artificially force a breakthrough of the brine from the injection chamber towards the lateral surface of the specimen, the pressure inside the injection chamber was step-wisely or by a defined pressure ramp increased until its desired level, which was agreed upon with the project partners prior to execution. During deformation of the sample and injection of the brine, the axial strain, pumped volume as well

as flowrate were also recorded (Figure 11). (3) Depending on the experimental duration, the injection pressure was either tried to be held constant after the breakthrough occurred or in case the injection pressure displayed a tremendous drop (from injection to atmospheric pressure ≤ 15 MPa), the piston of the utilized pump system used to control the injection pressure was held in constant position for a short period to investigate possible healing behavior. Here, after the healing period, the injection pressure was subsequently increased, if feasible. All samples have been tested for 50 (± 3) days (Table 3).

In general, the pressure inside the injection chamber necessary to create pathways (breakthrough) towards the lateral border of the specimens was either slightly below or even above the confining pressure (Table 3), which is indicative for a low permeable sample material at the given deformation conditions. Hence, this may be marking the onset of measurable permeable behavior. Typically, a breakthrough can be identified by a rapidly increasing brine volume being pumped into the injection chamber.

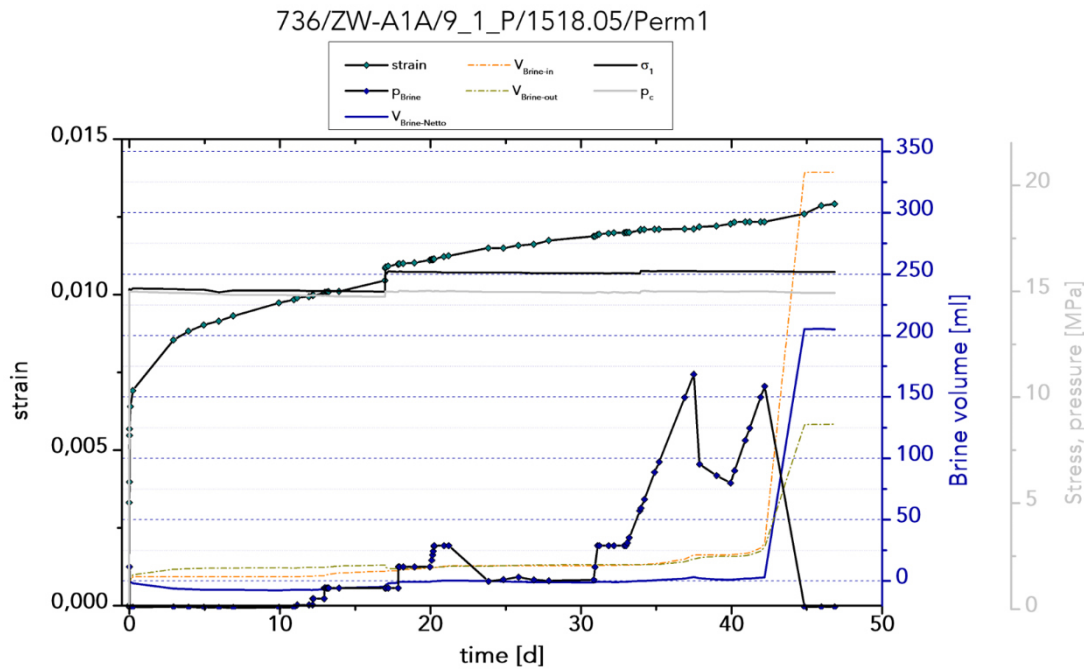


Figure 11: Creep curve including pumped brine volume as well as injection pressure recorded during deformation of sample 736/ZW/Perm1. During experimental deformation, temperature was held constant at $T = 40$ °C.

In the case of the specimen 736/ZW/Perm1, this may be observed at day 42 (Figure 11). Prior to the breakthrough, the injection pressure was only slightly increased in steps, at which no enhanced brine

volume has been pumped. However, after increasing the brine injection pressure (p_{Brine}) to a value of $p_{Brine} = 10.5$ MPa at a rate of 2MPa/d, the rate at which the volume of brine is being pumped into the injection chamber increases rapidly by more than one order of magnitude (Figure 11). Afterwards, the pressure was decreased to identify whether a potential healing may have occurred. This did not seem to be the case since increasing the injection pressure to the same value of $p_{Brine} = 10.5$ MPa was followed by dropping to atmospheric pressure, which led to stop the injection.

Compared to the results gathered from the creep tests, one may note an enhanced increase of strain over time, which may be due to the continuous usage of brine as well as a different geometry, especially in the vicinity of the borehole in the center of the sample. Therefore, comparing the deduced strain rates can misleading and should be done carefully.

Sample 736/ZW/Perm2 displays a somewhat contrasting behavior. Here, the injection chamber was also placed in the halite matrix, but with a layer of Anhydrite in its vicinity (Figure A 11a). After reaching (quasi) isostatic loading conditions and increasing the injection pressure at a rate of 0.4MPa/d, a breakthrough occurred at $p_{Brine} = 15.2$ MPa (day 26) (Figure A12a, Table 3) accompanied only with a minor drop of the injection pressure to $p_{Brine} = 14.65$ MPa. Trying to hold the injection pressure constant led to another tremendous increase in the flowrate (day 34). After a no-pumping period of four days, the injection pressure was increased again to a value of $p_{Brine} = 15$ MPa. Additionally, the axial load was increased to $\sigma_1 = 20$ MPa to avoid a bypass of the brine. Shortly afterwards another breakthrough occurred, resulting in a drop of the injection pressure to $p_{Brine} = 11.7$, which remained nearly constant during the pause phase (no pumping) of seven days. A final attempt of increasing the injection pressure at a rate 0.4 MPa/d yielded in another breakthrough at $p_{Brine} = 15$ MPa. Ultimately, the injection pressure dropped to a value of at $p_{Brine} = 12.3$ MPa at the end of the experiment. A clear indication as to where the breakthrough occurred was not visible by optical investigation of the deformed sample (Figure A 11b).

Specimen 736/ZW/Perm3 exhibited an entirely different loading path, which is believed to be induced by the coarse-grained halite matrix (Figure A 11c). At (quasi) isostatic conditions, increasing the injection pressure to $p_{Brine} = 15$ MPa at a rate of 0.4 MPa/d led to no occurrence of a breakthrough after four days. Only after increasing the pressure to $p_{Brine} = 16.4$ MPa at a rate of 0.1 MPa/d resulted in breakthrough (day 28) at which the pressure dropped to atmospheric conditions (Figure A12b). After a

resting phase of 14 days, we were able to increase the injection pressure to a value of $p_{Brine} = 2 \text{ MPa}$, indicating some healing processes within the sample may have been acted.

Sample 736/ZW/Perm4, where the injection chamber was placed partly along the transition from the Halite matrix into an Anhydrite formation (Figure A 11e) also displayed a unique behavior. Step wisely increasing the injection pressure to $p_{Brine} = 15.3 \text{ MPa}$ within 32 days did not lead to a clearly identifiable breakthrough of the brine as the flowrate remained nearly constant during that period. Holding the injection pressure constant at this value for seven days further increased the flowrate, but no pressure drop occurred. To remain sample integrity, the pumping phase was stopped (day 39), which followed by a progressively decreasing injection pressure to a final value of $p_{Brine} = 8 \text{ MPa}$ (Figure A12c).

Specimen 736/ZW/Perm5 contained almost no impurities but a solid, intact Halite matrix (Figure A 11g). After step-wisely and progressively increasing at a ramp of 2 MPa/d (day 22), the injection pressure reached a value of $p_{Brine} = 12 \text{ MPa}$ at which the flowrate did increase only slightly over a period of two days. Therefore, the pressure was further increased (0.4 MPa/d) up to $p_{Brine} = 12.8 \text{ MPa}$, which was accompanied by substantial increase of the flowrate. Pausing the injection for six days lead to pressure drop of $p_{Brine} = 10.8 \text{ MPa}$ (day 33). After this period the injection pressure was manually decreased to $p_{Brine} = 5 \text{ MPa}$ and held constant for five days, followed by a pressure ramp of 2 MPa/d up to $p_{Brine} = 12 \text{ MPa}$ again (day 41). Since no increasing flowrate could be observed for four days, the injection pressure was once again increased at a rate of 0.4 MPa/d to a value of $p_{Brine} = 13.6 \text{ MPa}$. The data shown in Figure A12d suggests that at this stage a breakthrough might have ultimately occurred. However, this observation could not be fully confirmed. After keeping the pore pressure system on hold, the injection pressure dropped to a final value of $p_{Brine} = 11.2 \text{ MPa}$.

Sample 736/ZW/Perm6 was mainly characterized by smaller Halite grains. The center of the specimen where the injection chamber was placed however, contained larger grains (Figure A 11i). These micro-structural features most likely are the reason for the loading path, which has been recorded during the deformation of the sample (Figure A12e). Step wisely increasing the injection pressure up to $p_{Brine} = 15.5 \text{ MPa}$ (day 38) only yielded some minor enhancements of the flowrate during this period. A breakthrough of the brine could not be observed during the following phase in which the injection has been kept constant.

4 SUMMARY

To characterize its mechanical as well as hydraulic properties, The *Institut für Gebirgsmechanik GmbH (IfG Leipzig)* was assigned by *Nobian* to execute an extensive laboratory test program on rock salt material belonging to the Zuidwending Cavern site. This incorporated additional microstructural investigations, which have been conducted by the *Microstructures and Pores GmbH (MaP)*, which acted as an additional partner to the overall project.

The task of *IfG Leipzig* can be summarized in performing three different types of experiments including their individual preparations regarding sample material as well as technical aspects. These three types comprise:

- (1) Pre-tests: gain basic knowledge on the mechanical properties of the investigated rock material.
- (2) Creep tests: unravel the long-term, time dependent mechanical properties of the rock salt material at representative conditions.
- (3) Permeability tests: quantify the hydraulic conductivity at elevated pressures and temperatures against brine.

The selection of suiting rock material was made prior to testing by *MaP* based on microstructural investigations and subsequently send to our laboratories. A detailed description of the investigated sample material as well as the experimental setup and used technique is provided in the paragraphs accordingly.

The results gained from the Pre-tests have been successfully implemented into the definition of boundary conditions applied during the performance of the planned creep experiments. Here, the main outcome is that the long-term creep behavior depends on microstructural features as well as applied deformational conditions, especially the applied axial differential stress. All samples except for one displayed ductile deformation behavior with the ability to compensate deformation at axial strains beyond values of 20% by barreling and some bulging, which was individual to each sample and most likely driven by its microstructural features. One sample may have shown a slight transition from ductile towards more brittle behavior, which was expressed by the formation of inclined shear fracture upon deformation. However, more detailed microstructural evidence is necessary to proof this observation

(personal communication with *MaP*). Regarding its ability to conduct brine, the performed experiments lead to suggest that the investigated rock salt material is characterized by low hydraulic properties as almost no brine flow could be realized at low injection pressures. Regarding intact sample material, only after exceeding the applied axial and radial stresses, the brine was able to flow either along grain boundaries or internal interlayers (Anhydrite layers). However, it was also shown that mechanical as well as microstructural features (fractures, mineral transition zones) can alter the tightness of the investigated sample material. It should be noted that a (partial) recovery of the sample's initial conductive properties (healing) could be observed in some cases.

All samples tested and deformed in addition to powder material were sent to *MaP* for further micro-structural investigations as well as geochemical analyses. Additionally, four samples deformed by Pre-testing have been sent to the Underground Research Laboratory in the Altaussee mine (AT) for further creep testing under controlled in situ deformation conditions.

REFERENCES

- ASTM International. (1996). Standard Test Method for Triaxial Compressive Strength of Undrained Rock Core Specimens Without Pore Pressure Measurements. *ASTM International*.
- ASTM International. (1998). Standard Test Method for Creep of Rock Core Specimens in Triaxial Compression at Ambient or Elevated Temperatures. *ASTM International*. www.astm.org,
- ASTM International. (2001). Standard Practices for Preparing Rock Core Specimens and Determining Dimensional and Shape Tolerances. *ASTM International*.
- ASTM International. (2002). Standard Test Methods for X-Ray Radiography of Soil Samples. *ASTM International*.
- ASTM International. (2004). Standard Test Method for Creep of Rock Core Under Constant Stress and Temperature. *ASTM International*. www.astm.org
- ASTM International. (2005). Standard Test Method for Laboratory Determination of Pulse Velocities and Ultrasonic Elastic Constants of Rock. *ASTM International*. www.astm.org
- ASTM International. (2016). Standard Test Methods for Creep of Rock Core Under Constant Stress and Temperature. *ASTM International*. <https://doi.org/10.1520/D7070-16>
- Atangana, A. (2018). Principle of Groundwater Flow. *Fractional Operators with Constant and Variable Order with Application to Geo-Hydrology*, 15–47. <https://doi.org/10.1016/B978-0-12-809670-3.00002-3>
- Bérest, P., Gharbi, H., Brouard, B., Brückner, D., DeVries, K., Hévin, G., Hofer, G., Spiers, C., & Urai, J. (2019). Very Slow Creep Tests on Salt Samples. *Rock Mechanics and Rock Engineering*, 52(9), 2917–2934. <https://doi.org/10.1007/s00603-019-01778-9>
- Herrmann, J., Naumann, D., & Rölke, C. (2023). *Rock Mechanical Investigations on Rock Salt Samples recovered from the Heiligerlee Cavern Site, Test Results and Parameter Evaluation*.
- Rutter, E. H. (1986). On the nomenclature of mode of failure transitions in rocks. *Tectonophysics*, 122, 381–387.
- Strohmenger, C., Voigt, E., & Zimdars, J. (1996). Sequence stratigraphy and cyclic development of Basal Zechstein carbonate-evaporite deposits with emphasis on Zechstein 2 off-platform carbonates (Upper Permian, Northeast Germany). *Sedimentary Geology*, 102(1–2), 33–54. [https://doi.org/10.1016/0037-0738\(95\)00058-5](https://doi.org/10.1016/0037-0738(95)00058-5)
- Ulusay, R., & Hudson, J. (2015). *The Complete ISRM Suggested Methods for Rock Characterization, Testing and Monitoring: 1974-2006* (R. Ulusay & J. Hudson, Eds.). Springer International Publishing.

APPENDIX



A1: Specimens – Pre-Tests I-I

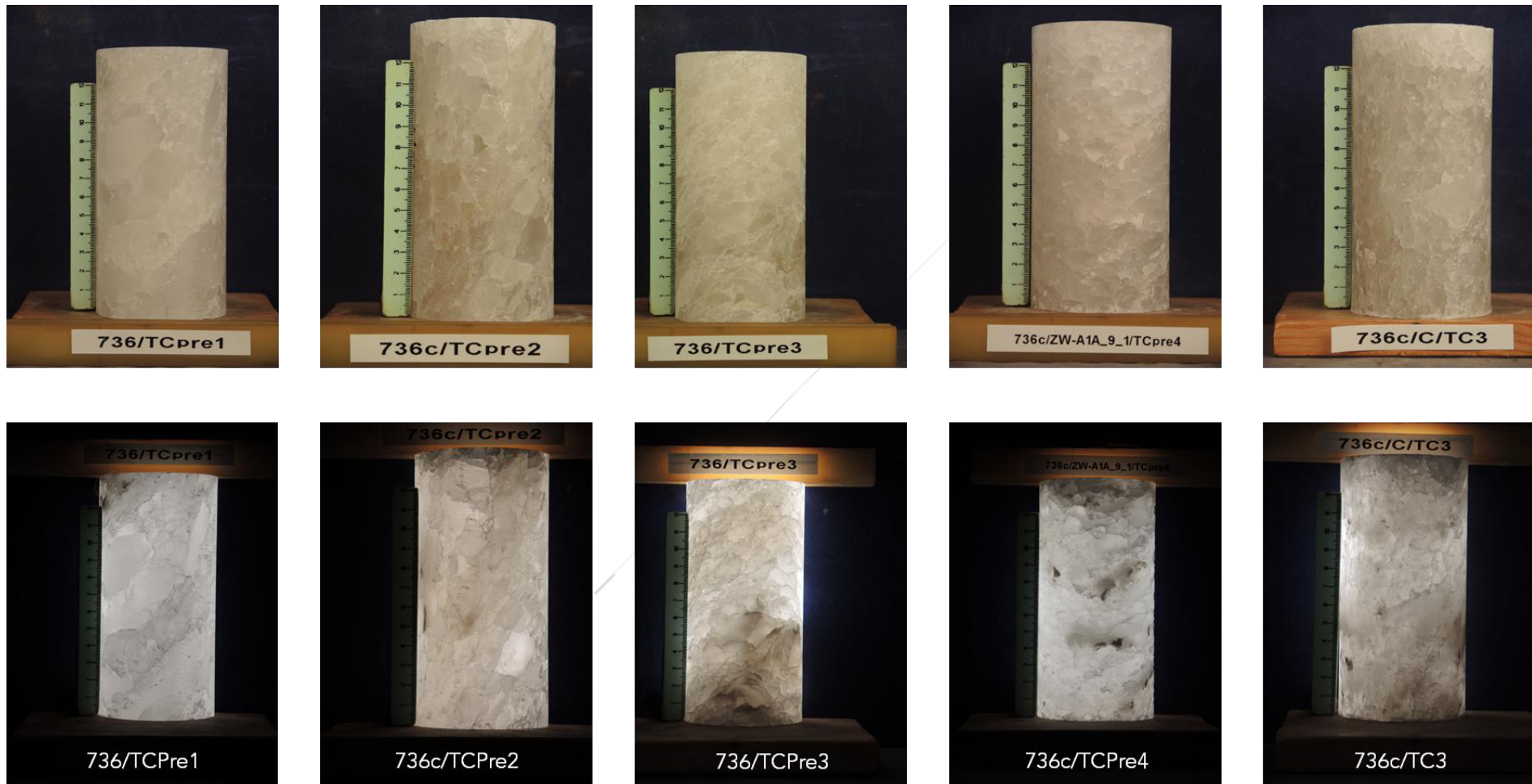


Figure A1: Prepared specimens prior to pre-testing at normal and transmissive lighting conditions (part I).

A2: Specimens – Pre-Tests I-II

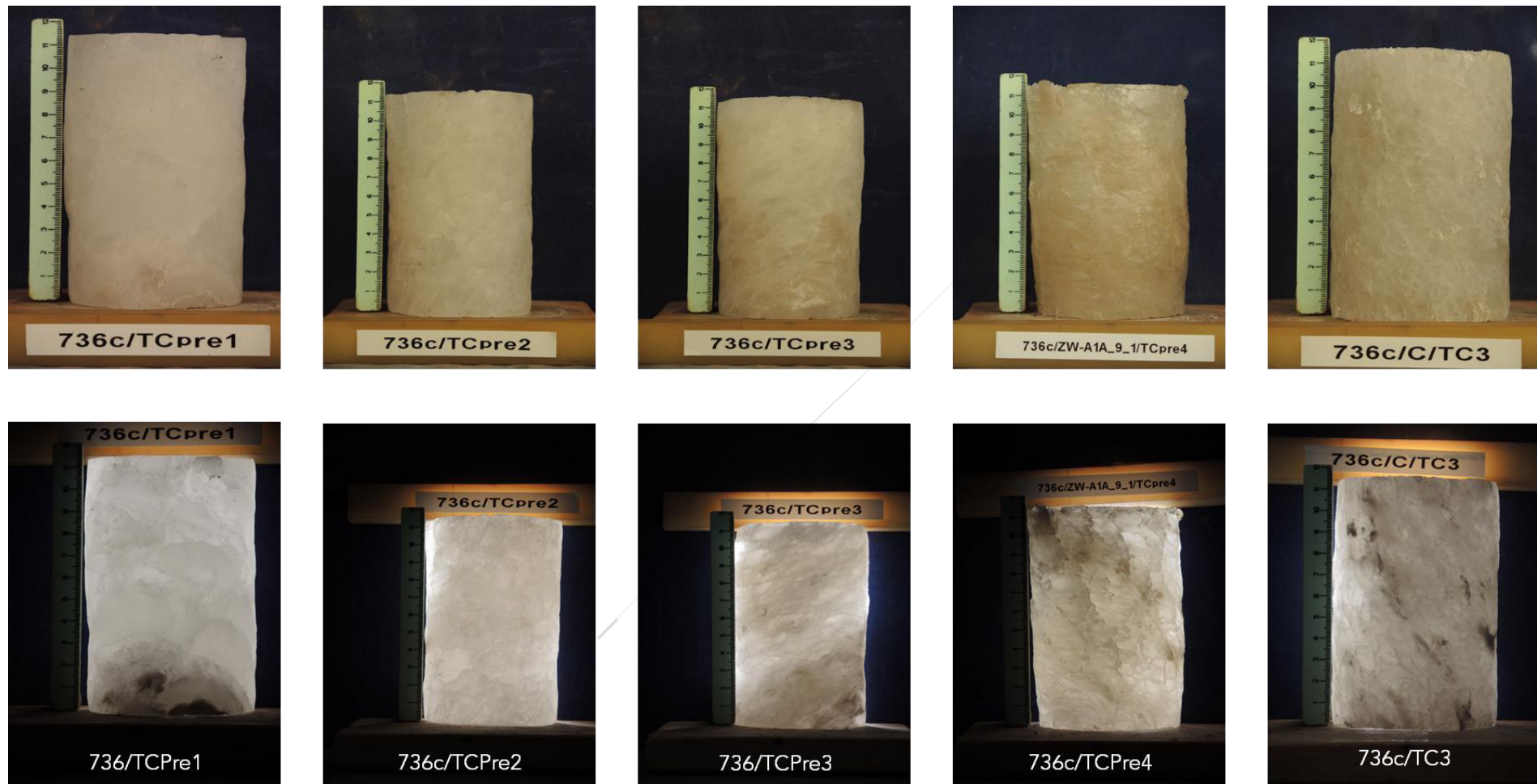


Figure A2: Prepared specimens after pre-testing at normal and transmissive lighting conditions.

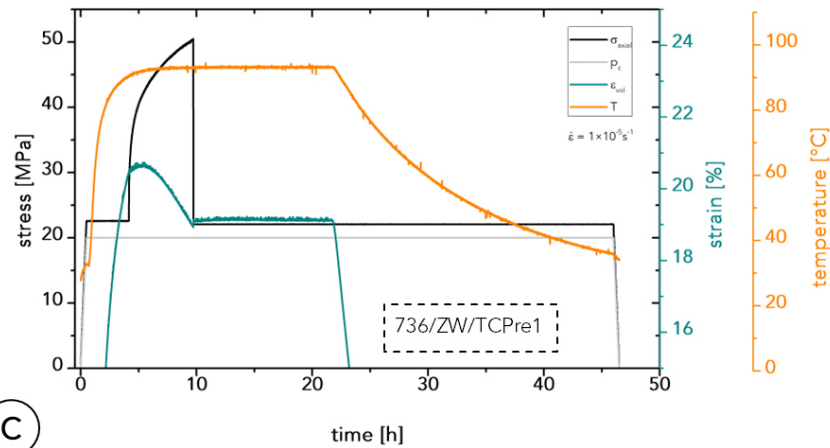
A3: Specimens – Pre-Tests II



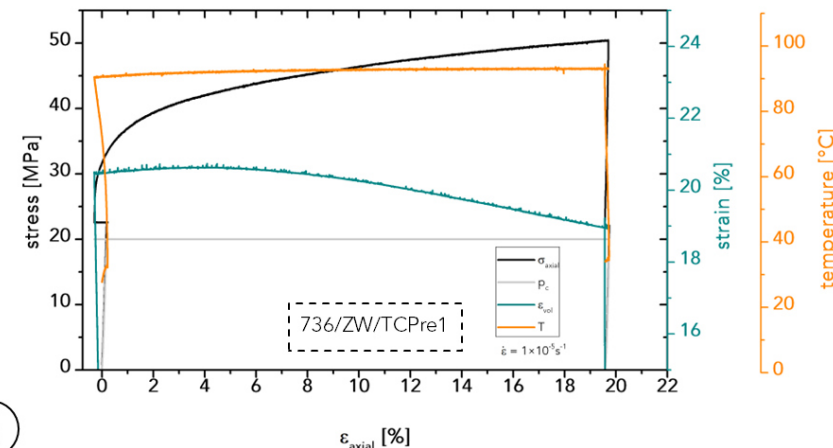
Figure A3: Prepared specimens prior to pre-testing at normal and transmissive lighting conditions (part II).

A4: Pre-Tests – Experimental protocol and stress-strain behavior

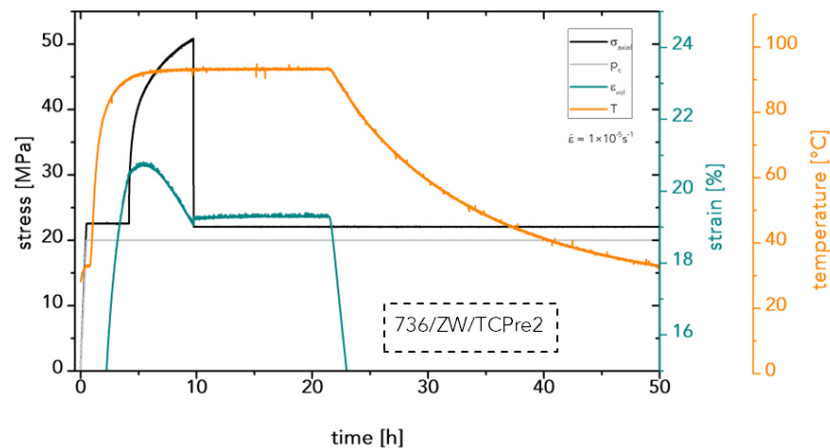
(a)



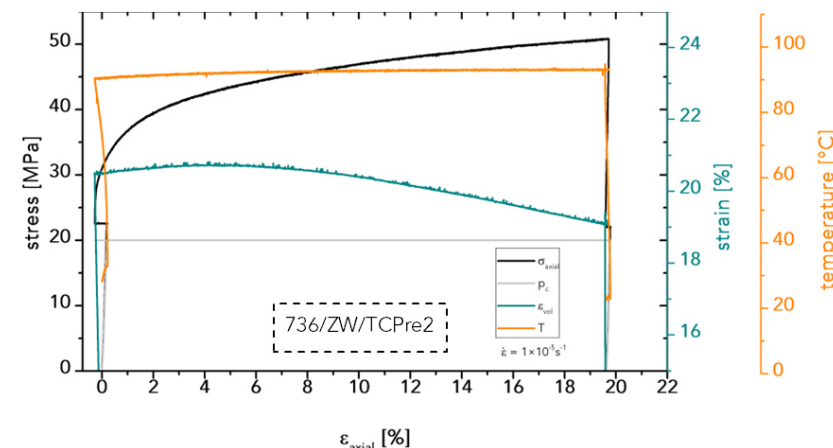
(b)



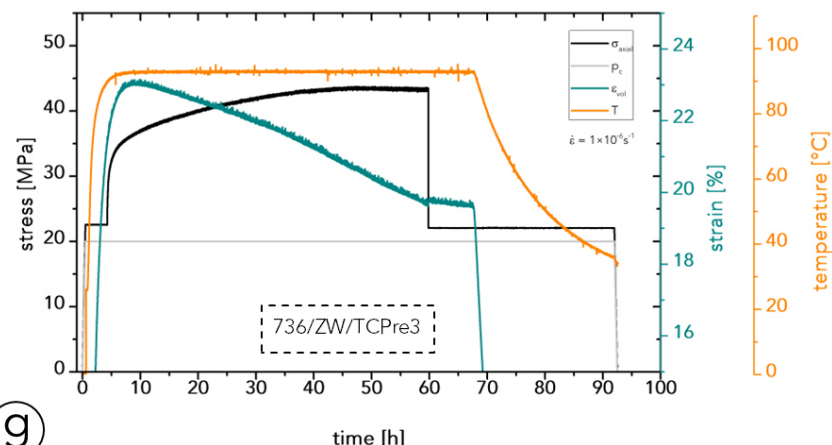
(c)



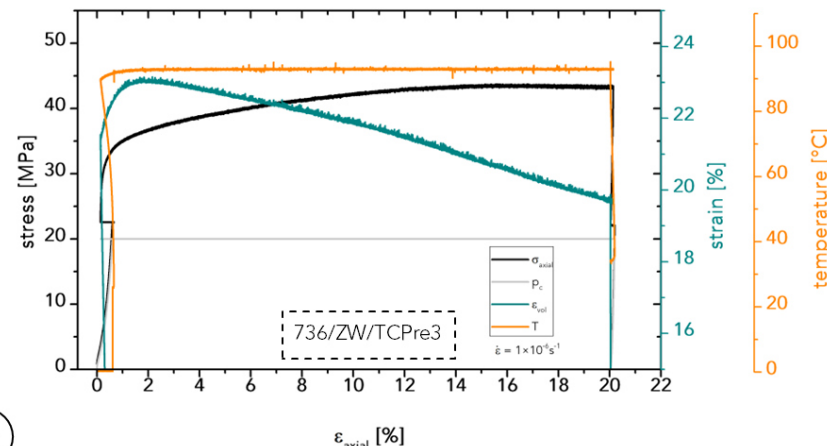
(d)



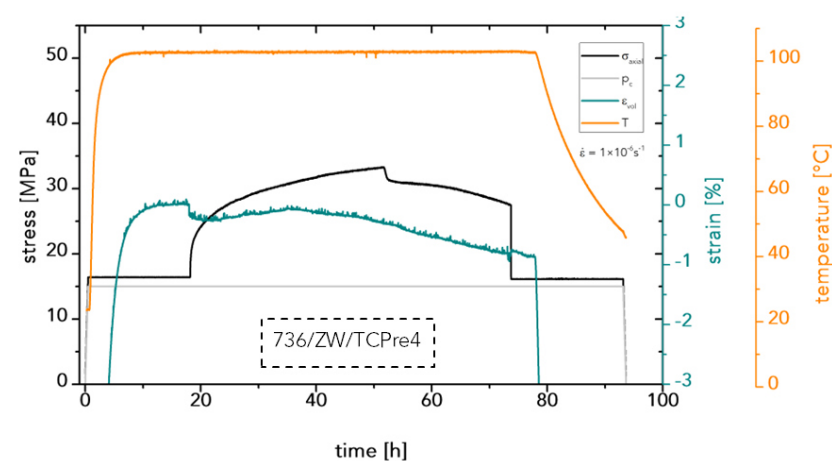
(e)



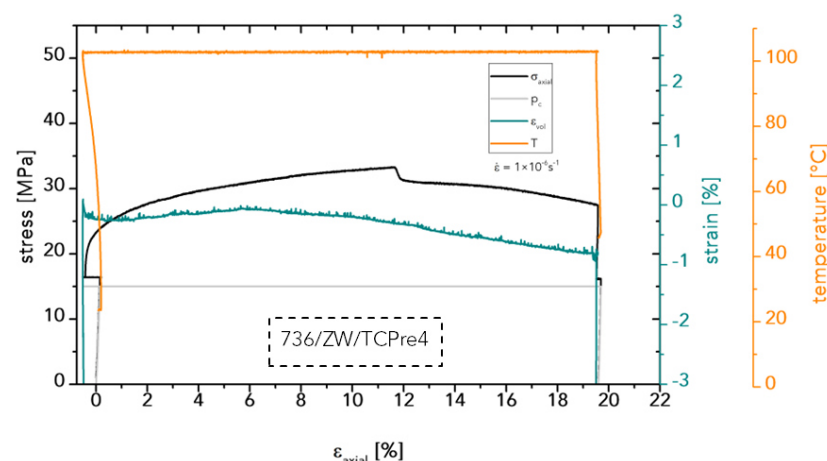
(f)



(g)



(h)



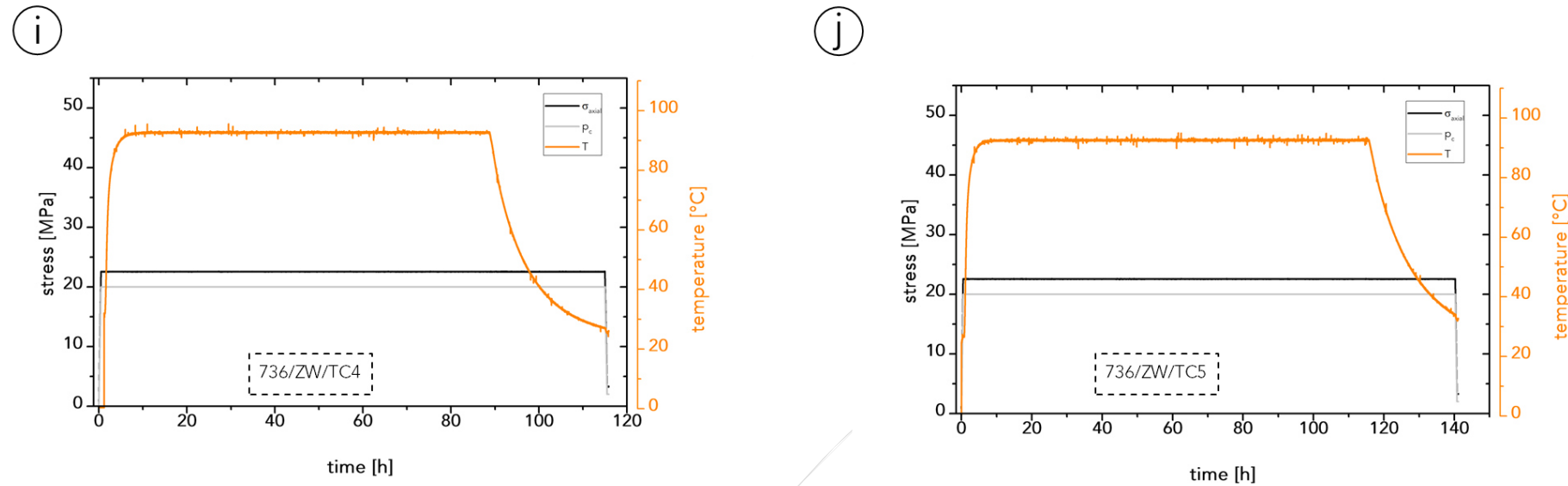


Figure A4: Experimental protocol (a, c, e, g, i, j) and recorded stress – strain curves (including volumetric strain) of the deformed samples (b, d, f, h). Sample descriptions are indicated.

A5: Specimens - creep experiments I-I

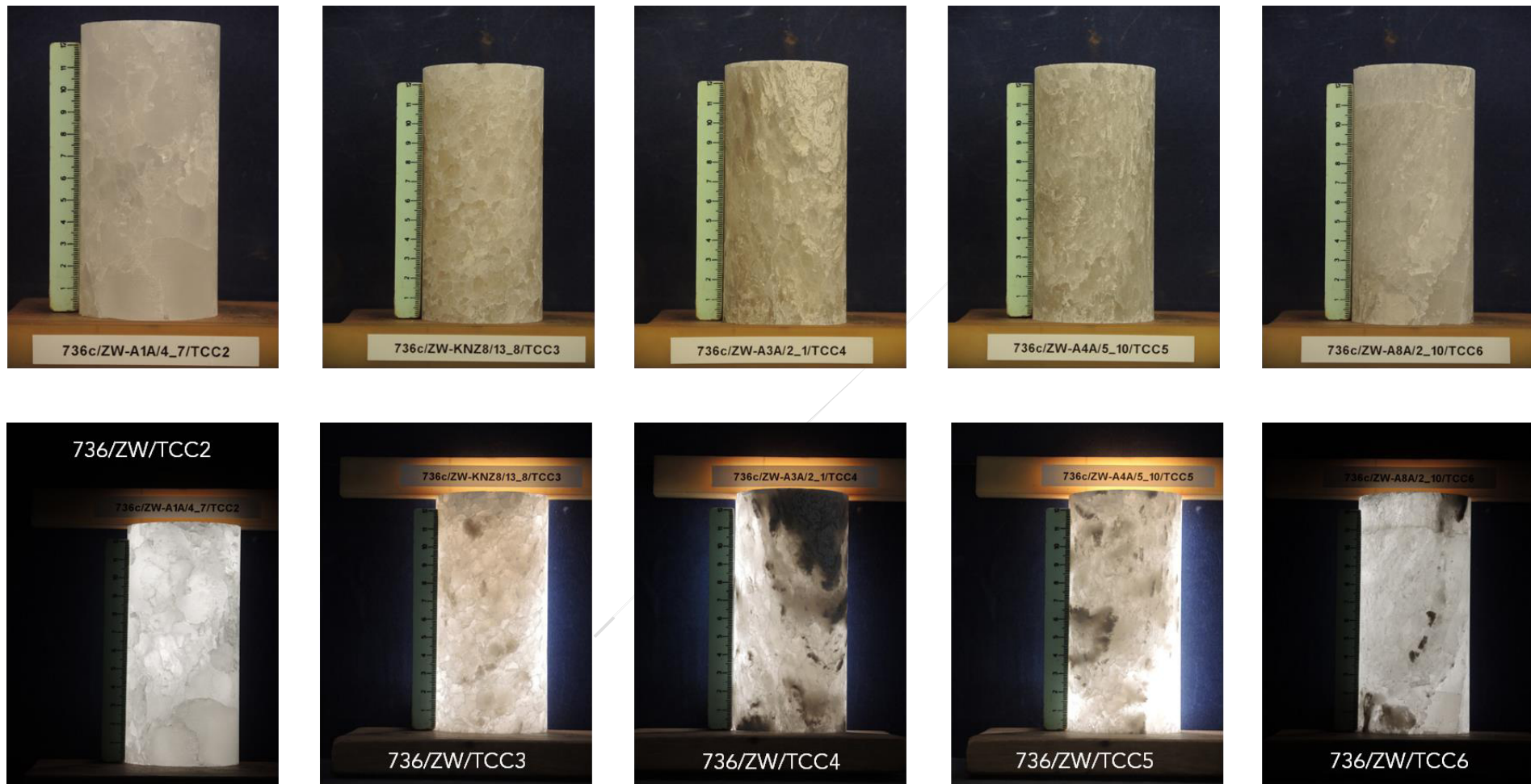


Figure A5: Prepared specimens prior to creep testing at normal and transmissive lighting conditions (part I-I).

A6: Specimens – creep experiments I-II

before



after

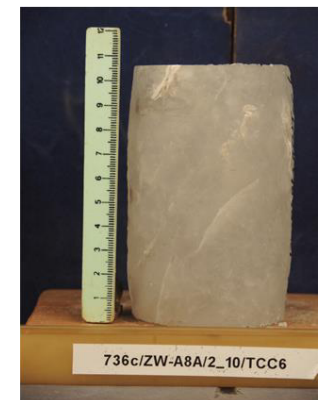


Figure A6: Prepared specimens before and after creep testing (part I-II).

A7: Specimens - creep experiments II-I

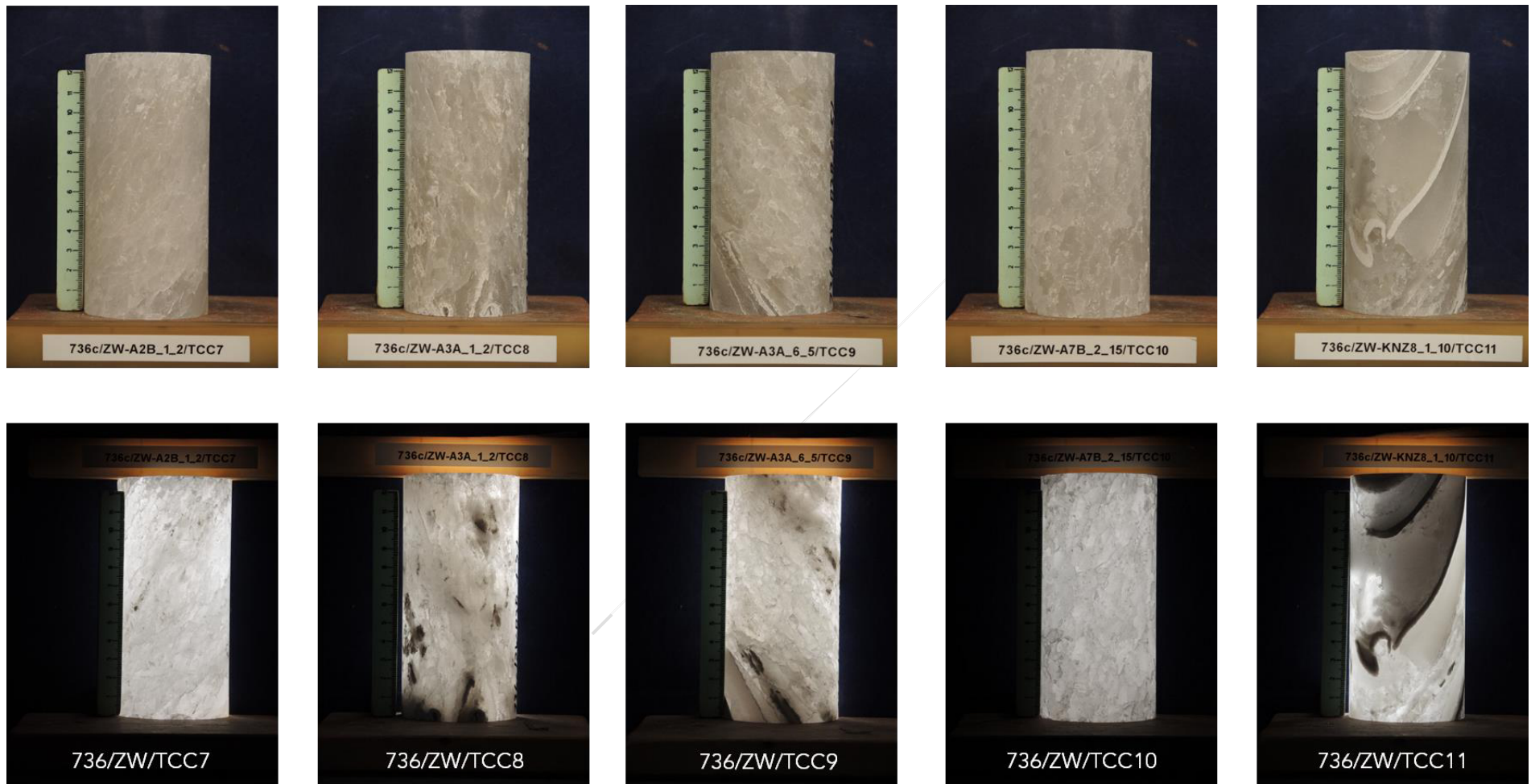


Figure A7: Prepared specimens prior to creep testing at normal and transmissive lighting conditions (part II-I).

A8: Specimens - creep experiments II-II

before



after



Figure A8: Prepared specimens before and after creep testing (part II-II).

A9: Specimens - creep experiments III



Figure A9: Prepared specimen before and after creep testing (part III).

A10: Recorded creep curves during deformation

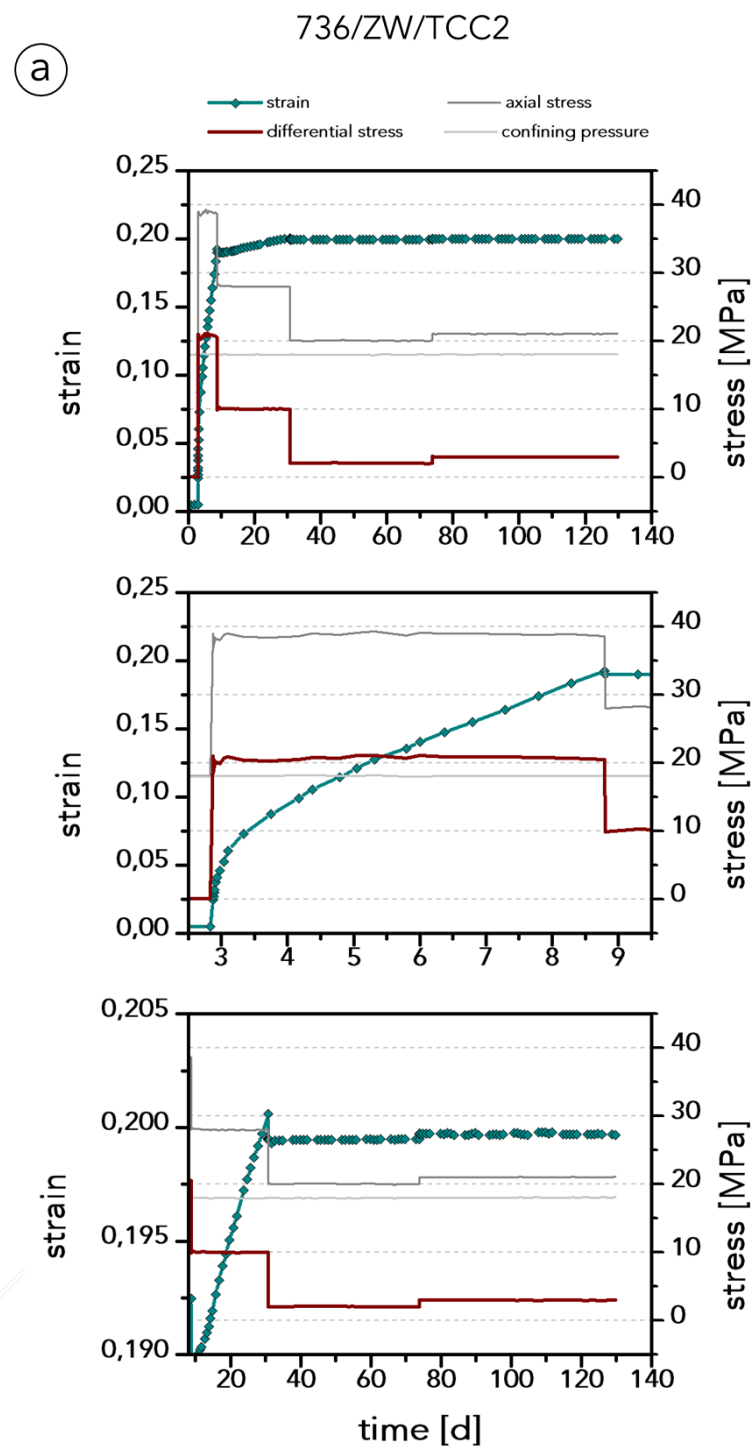
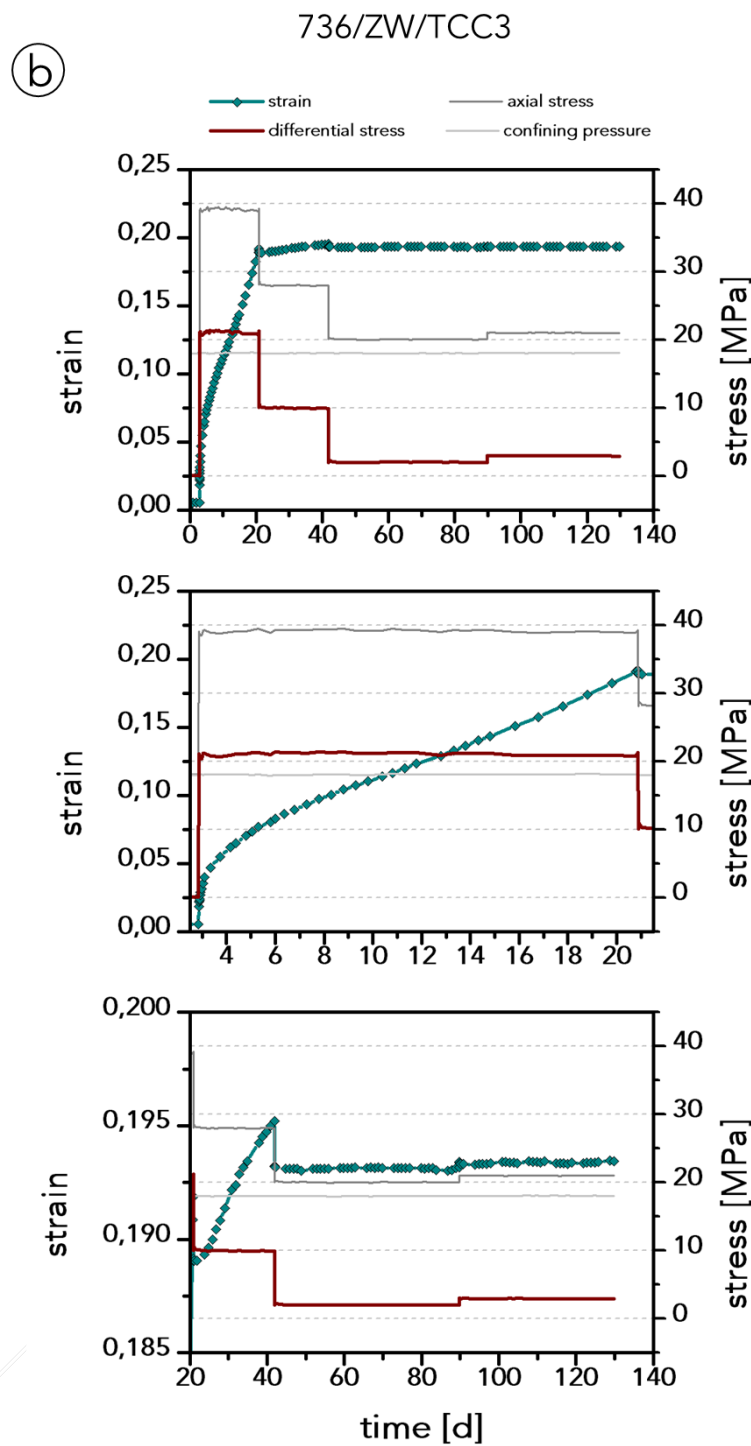
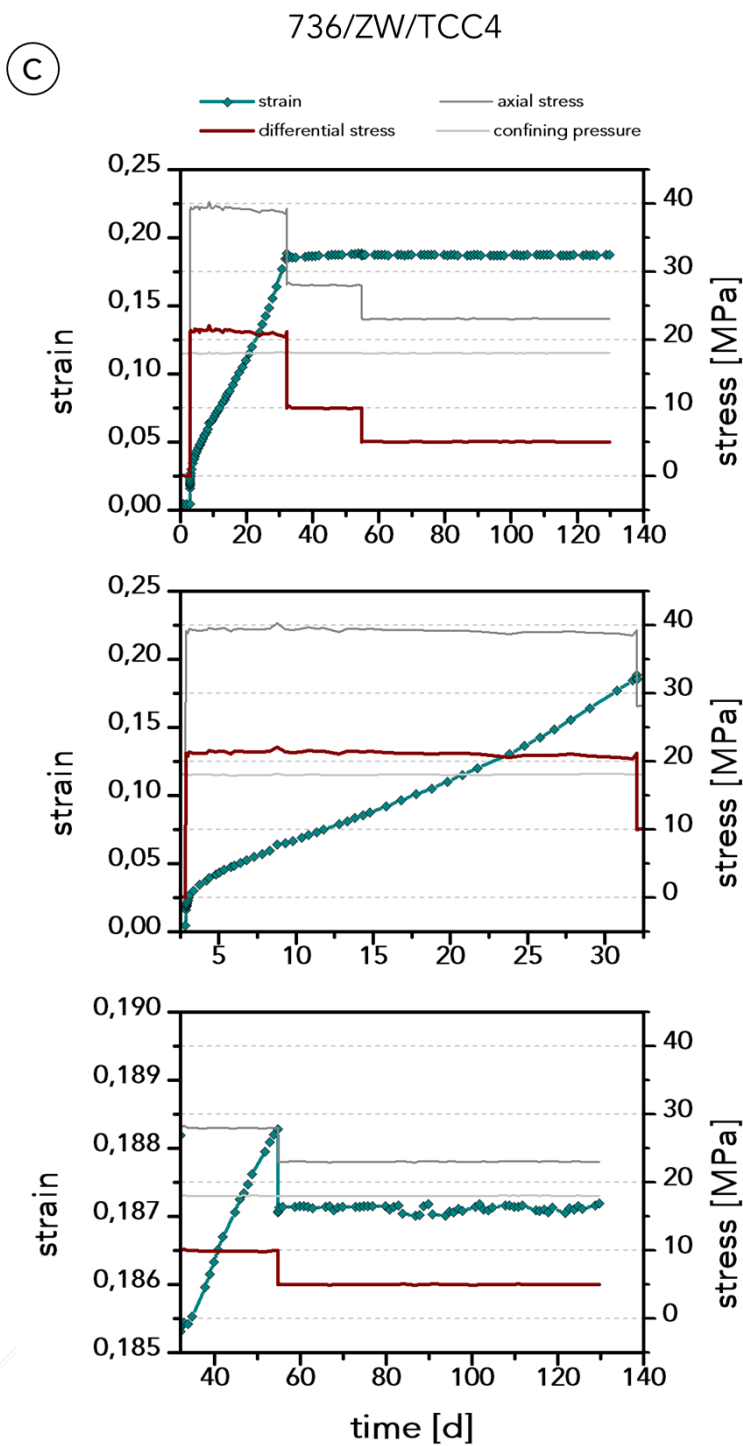


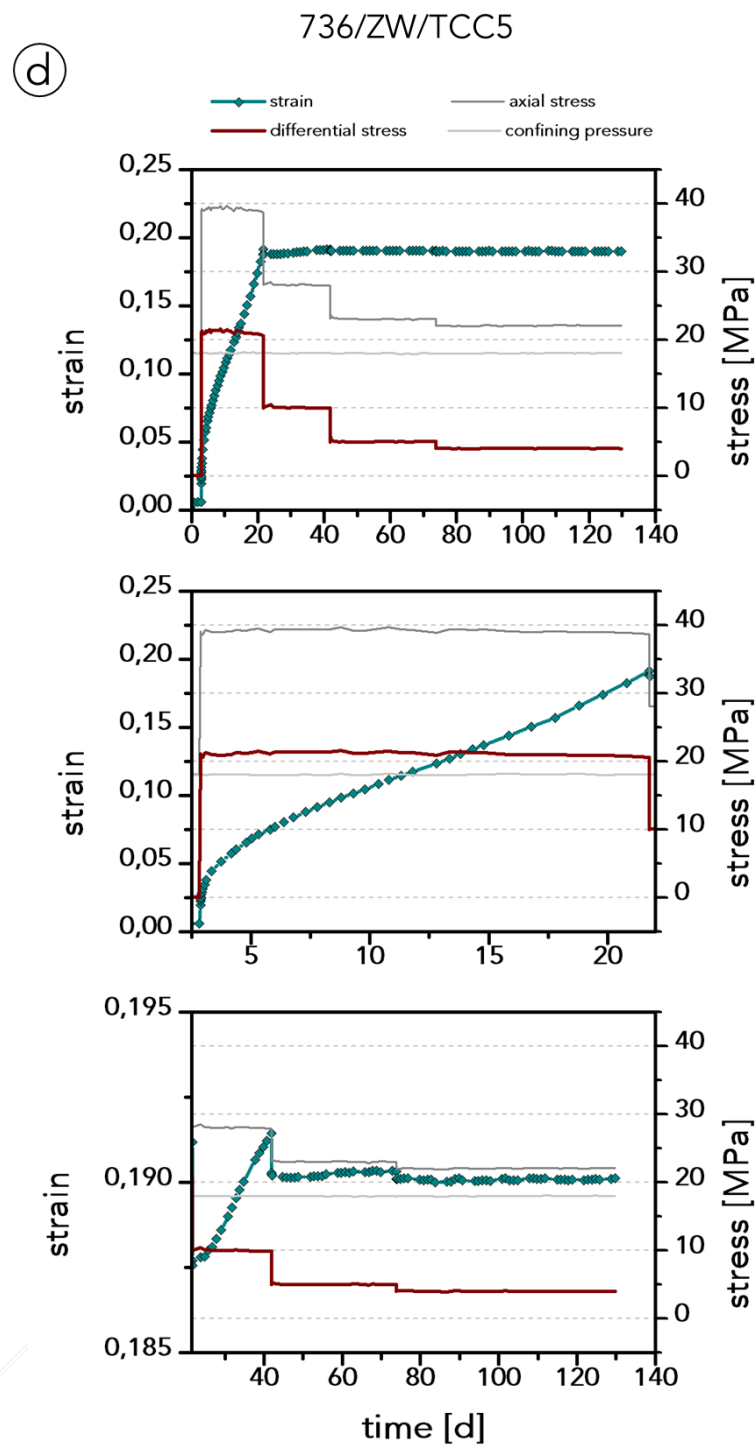
Figure A10: (a) Creep curve recorded during deformation of sample 736/ZW/TCC2. During experimental deformation, temperature was held constant at $T = 100\text{ }^{\circ}\text{C}$.



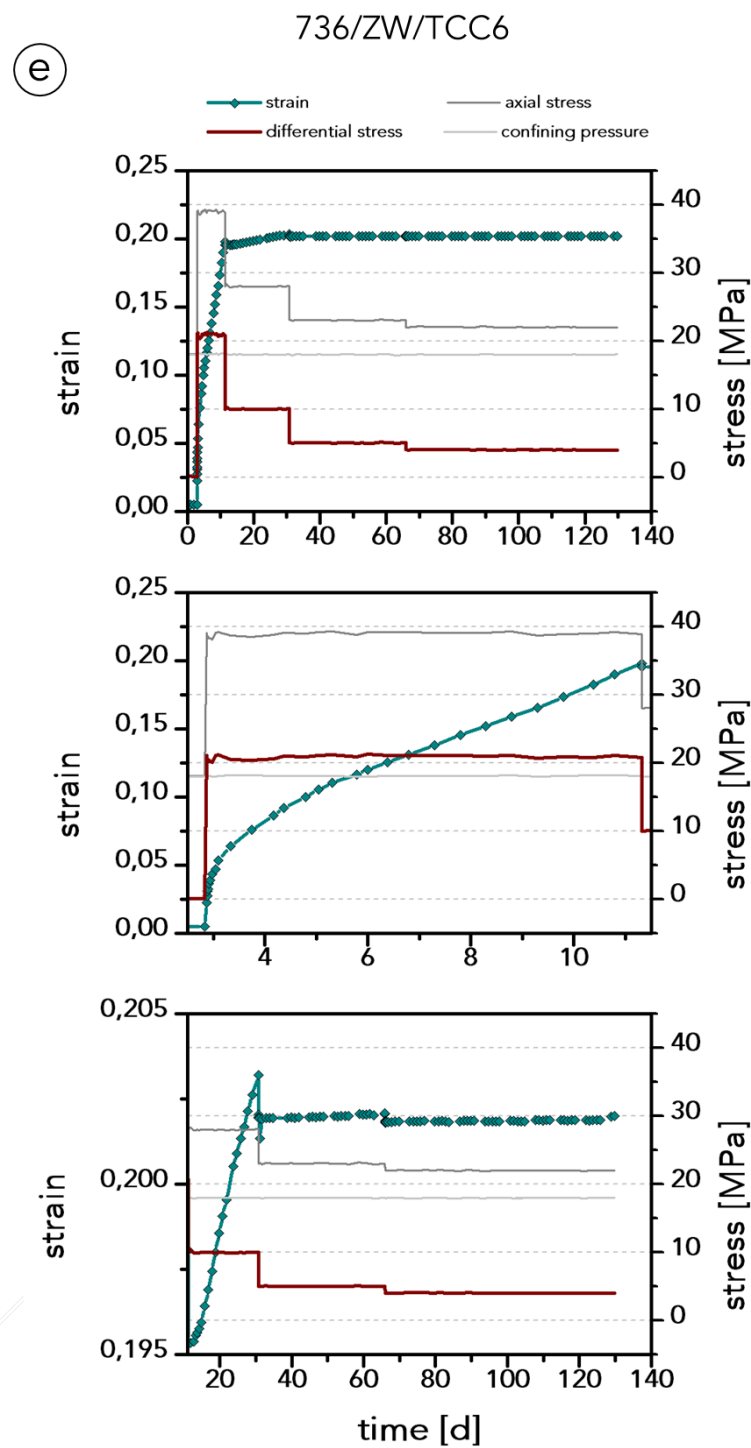
(b) Creep curve recorded during deformation of sample 736/ZW/TCC3. During experimental deformation, temperature was held constant at $T = 100\text{ }^{\circ}\text{C}$.



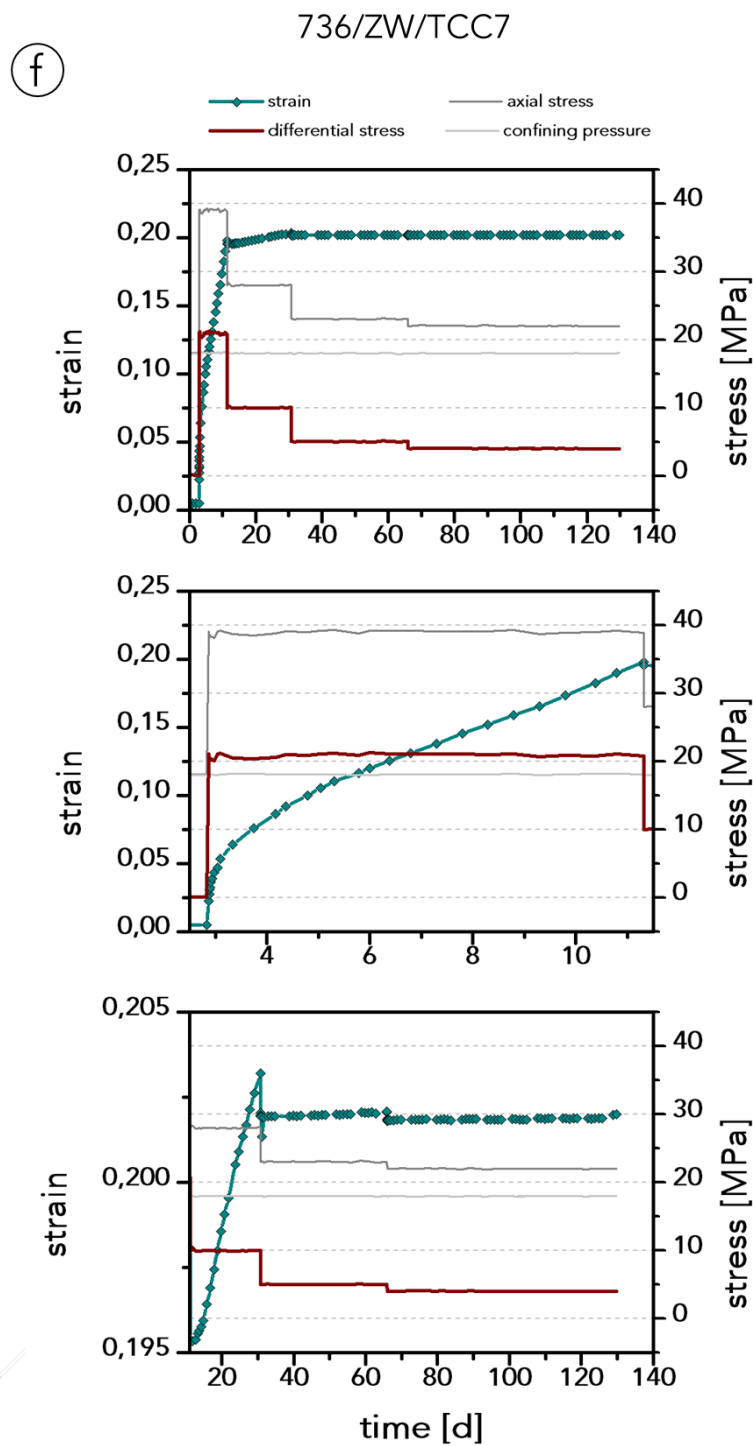
(c) Creep curve recorded during deformation of sample 736/ZW/TCC4. During experimental deformation, temperature was held constant at $T = 100\text{ }^{\circ}\text{C}$.



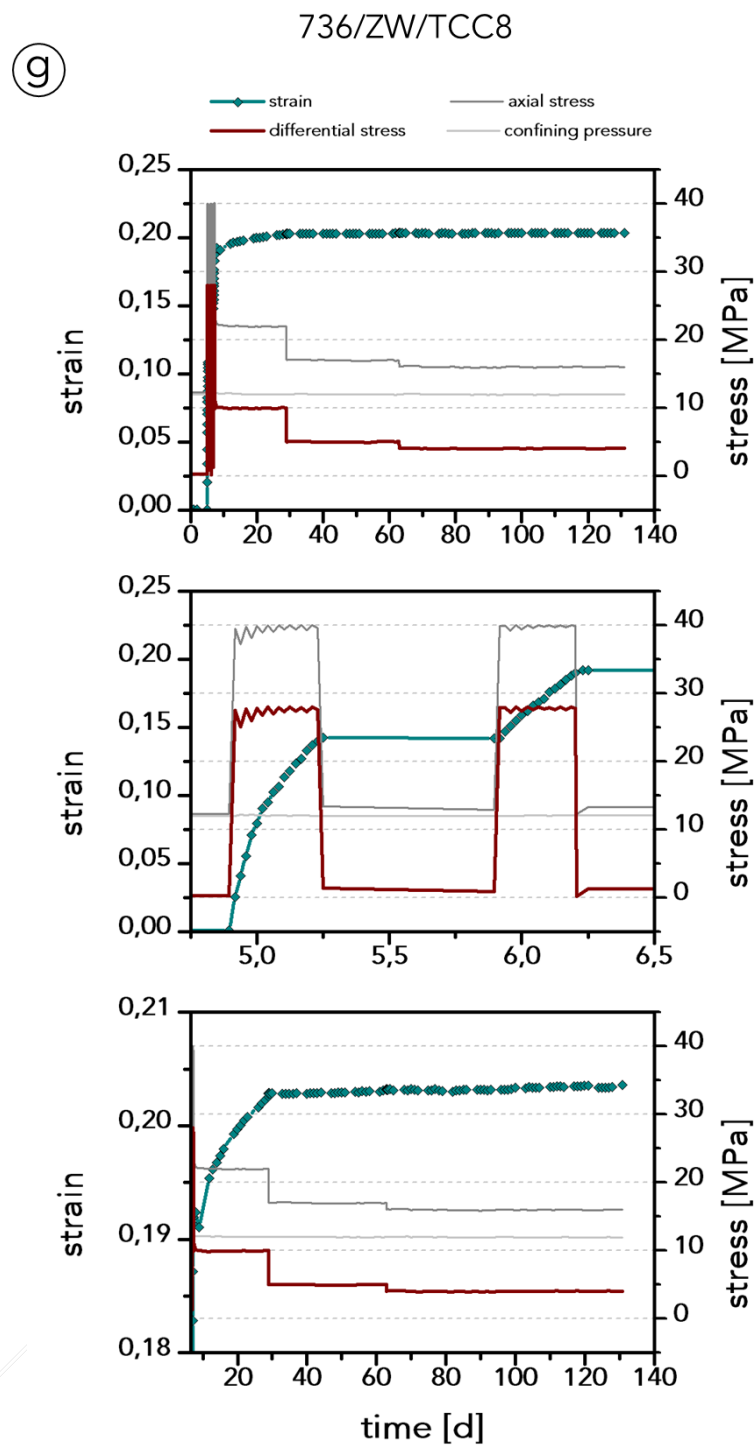
(d) Creep curve recorded during deformation of sample 736/ZW/TCC5. During experimental deformation, temperature was held constant at $T = 100\text{ }^{\circ}\text{C}$.



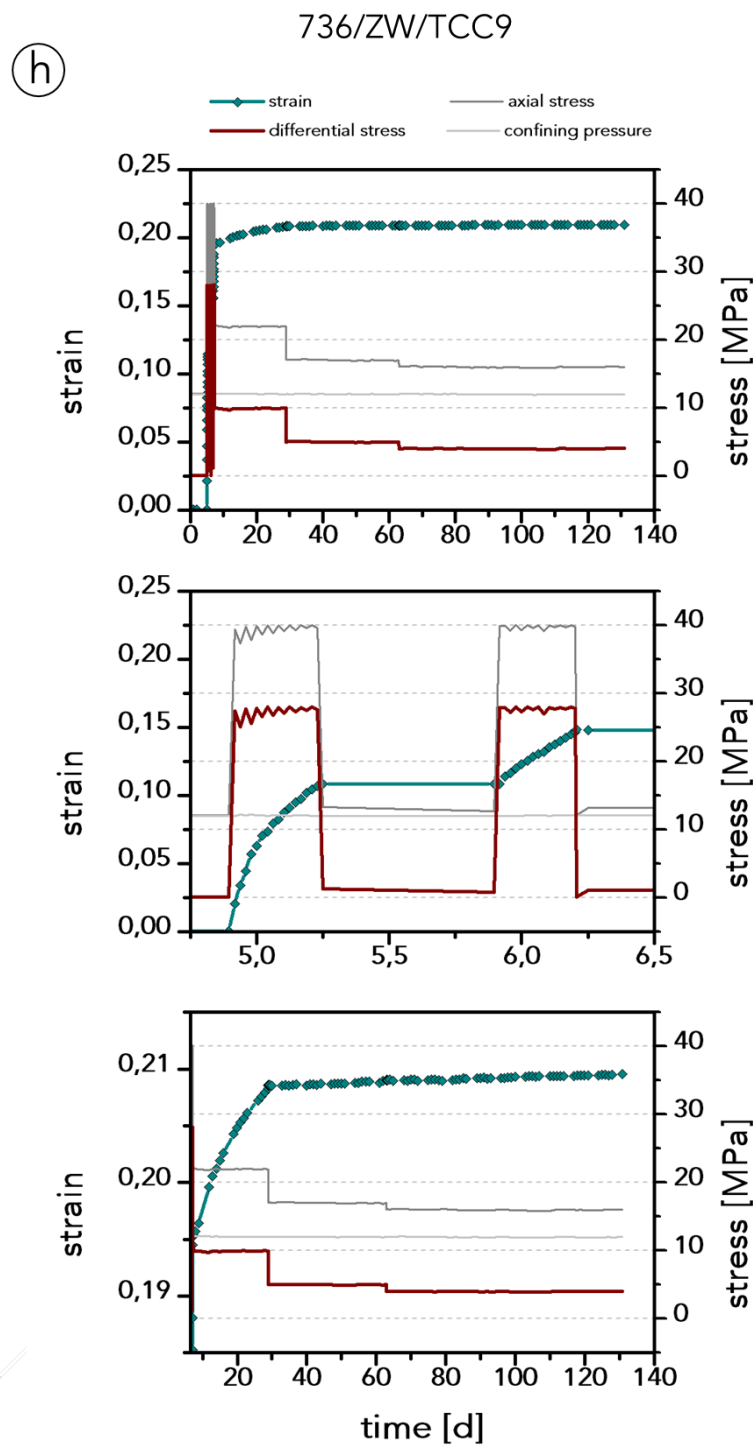
(e) Creep curve recorded during deformation of sample 736/ZW/TCC6. During experimental deformation, temperature was held constant at $T = 100\text{ }^{\circ}\text{C}$.



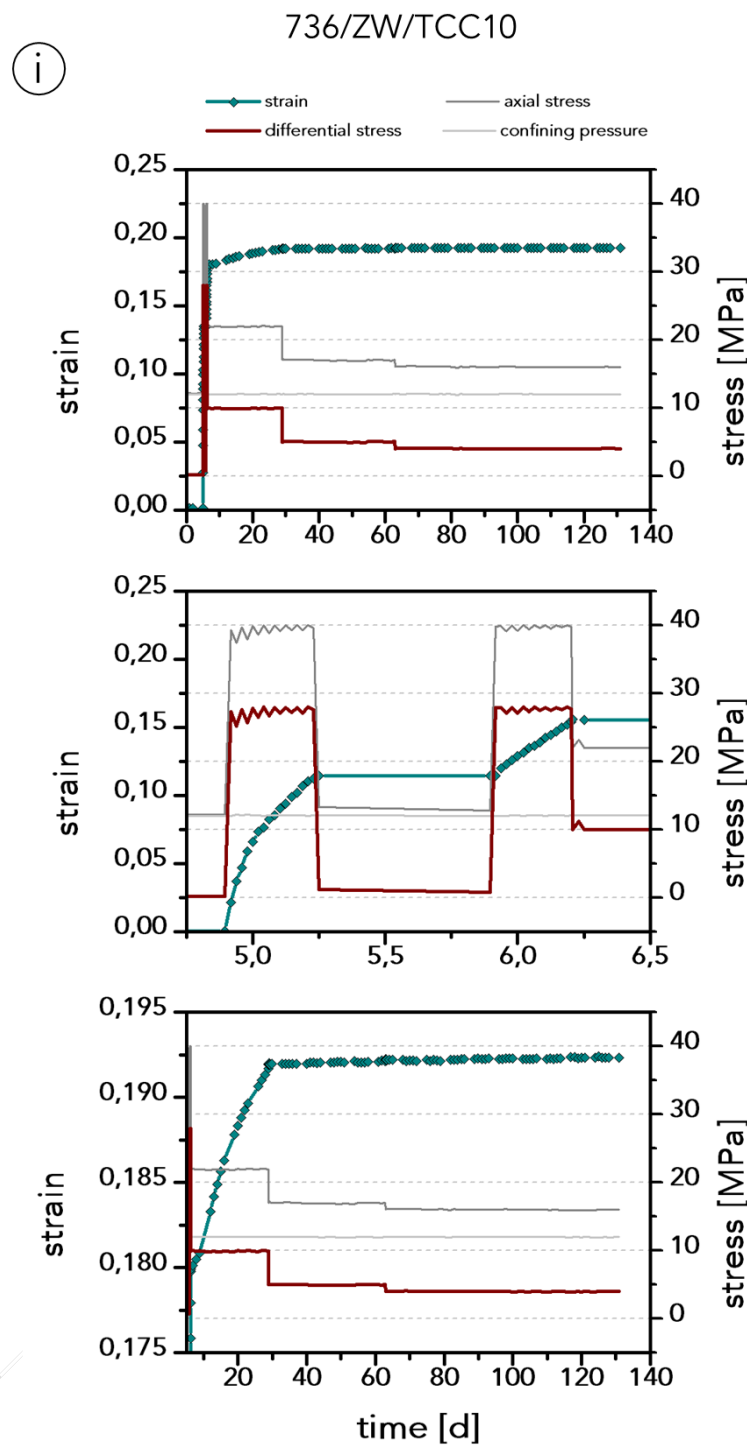
(f) Creep curve recorded during deformation of sample 736/ZW/TCC7. During experimental deformation, temperature was held constant at $T = 100^\circ\text{C}$.



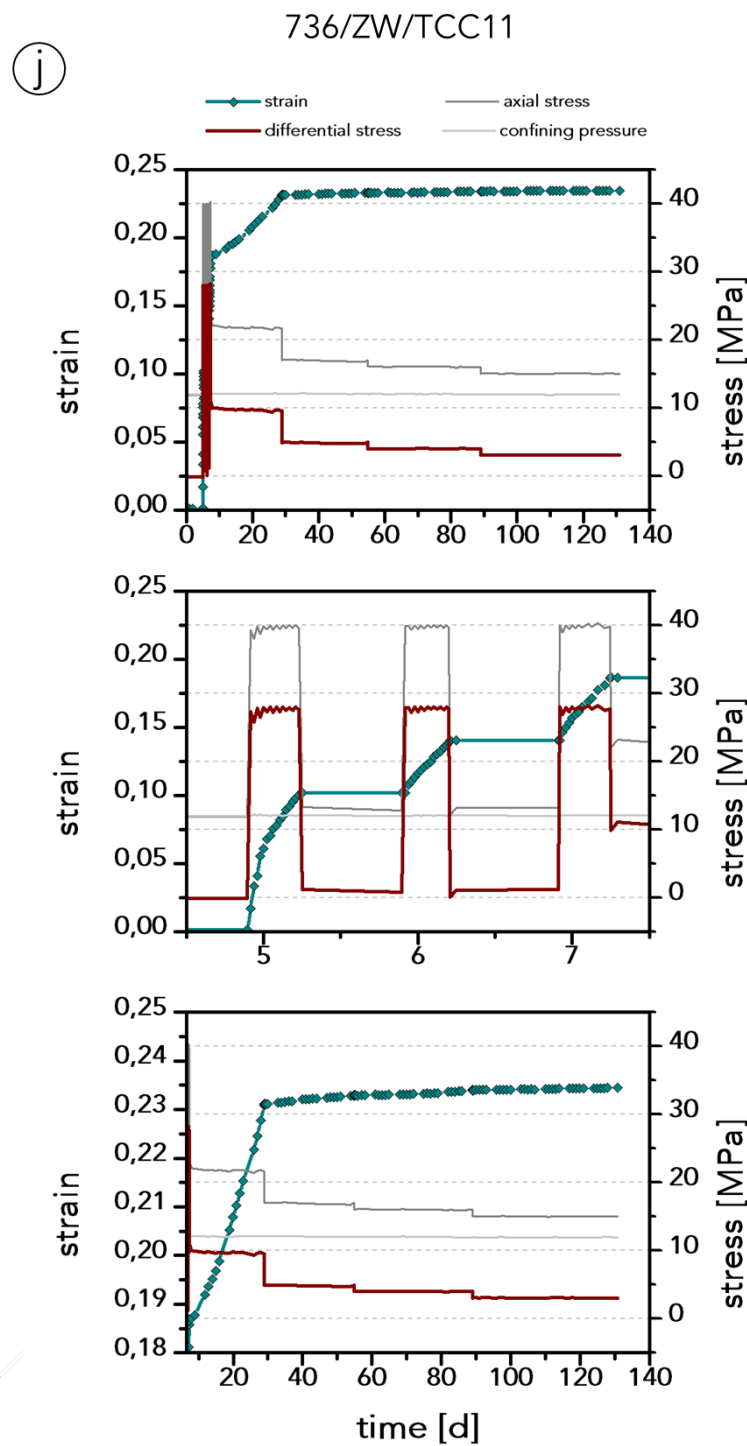
(g) Creep curve recorded during deformation of sample 736/ZW/TCC8. During experimental deformation, temperature was held constant at $T = 100\text{ }^{\circ}\text{C}$.



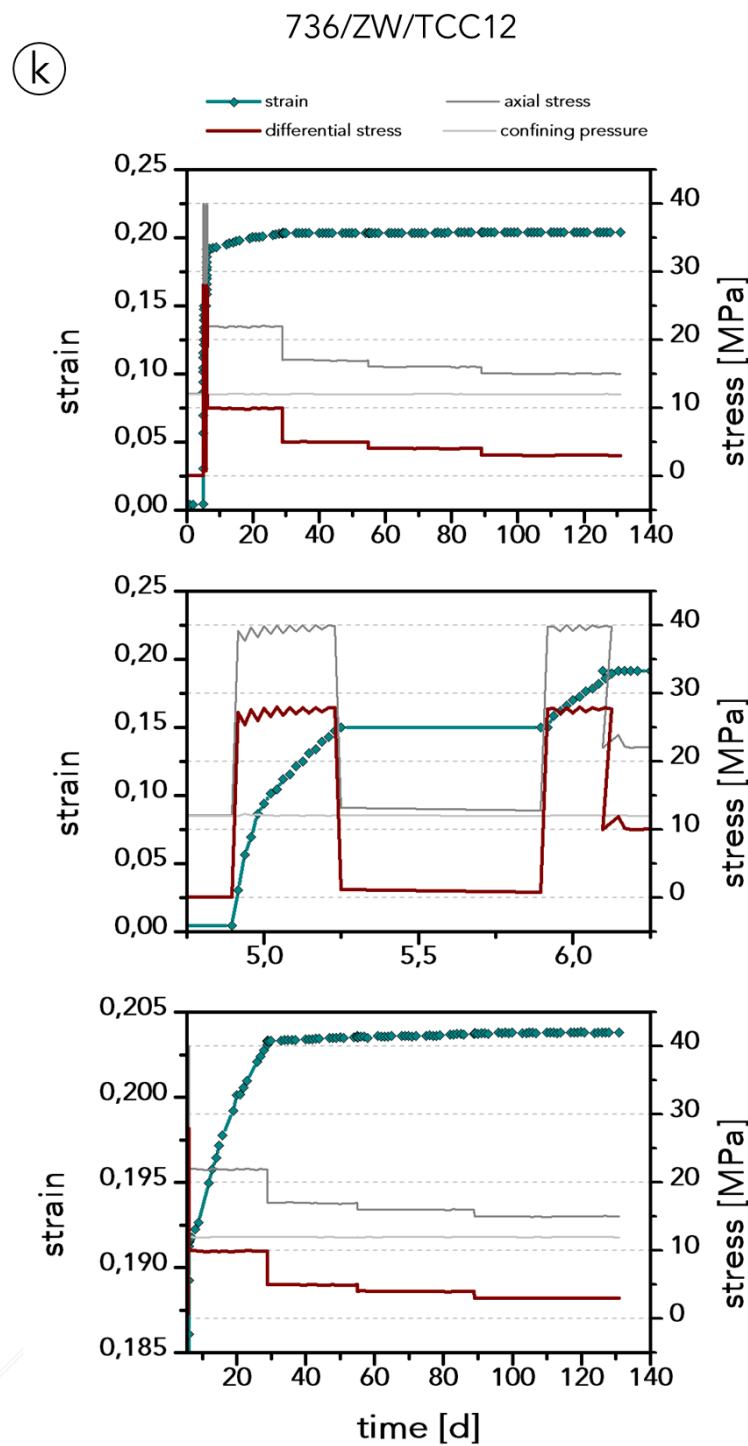
(h) Creep curve recorded during deformation of sample 736/ZW/TCC9. During experimental deformation, temperature was held constant at $T = 100\text{ }^{\circ}\text{C}$.



(i) Creep curve recorded during deformation of sample 736/ZW/TCC10. During experimental deformation, temperature was held constant at $T = 100\text{ }^{\circ}\text{C}$.

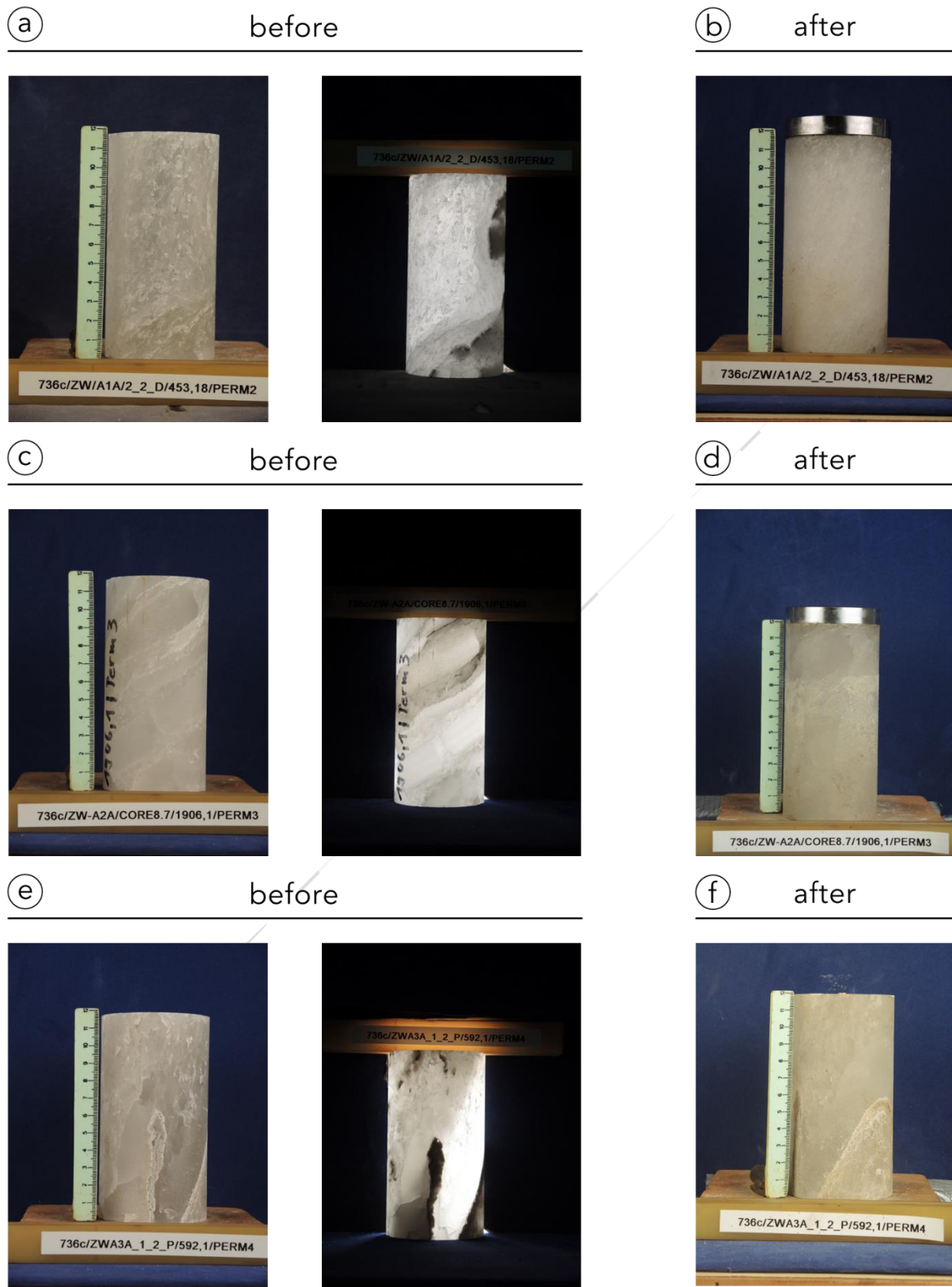


(j) Creep curve recorded during deformation of sample 736/ZW/TCC11. During experimental deformation, temperature was held constant at $T = 100\text{ }^{\circ}\text{C}$.



(k) Creep curve recorded during deformation of sample 736/ZW/TCC12. During experimental deformation, temperature was held constant at $T = 100\text{ }^{\circ}\text{C}$.

A11: Samples prepared for hydraulic conductivity testing



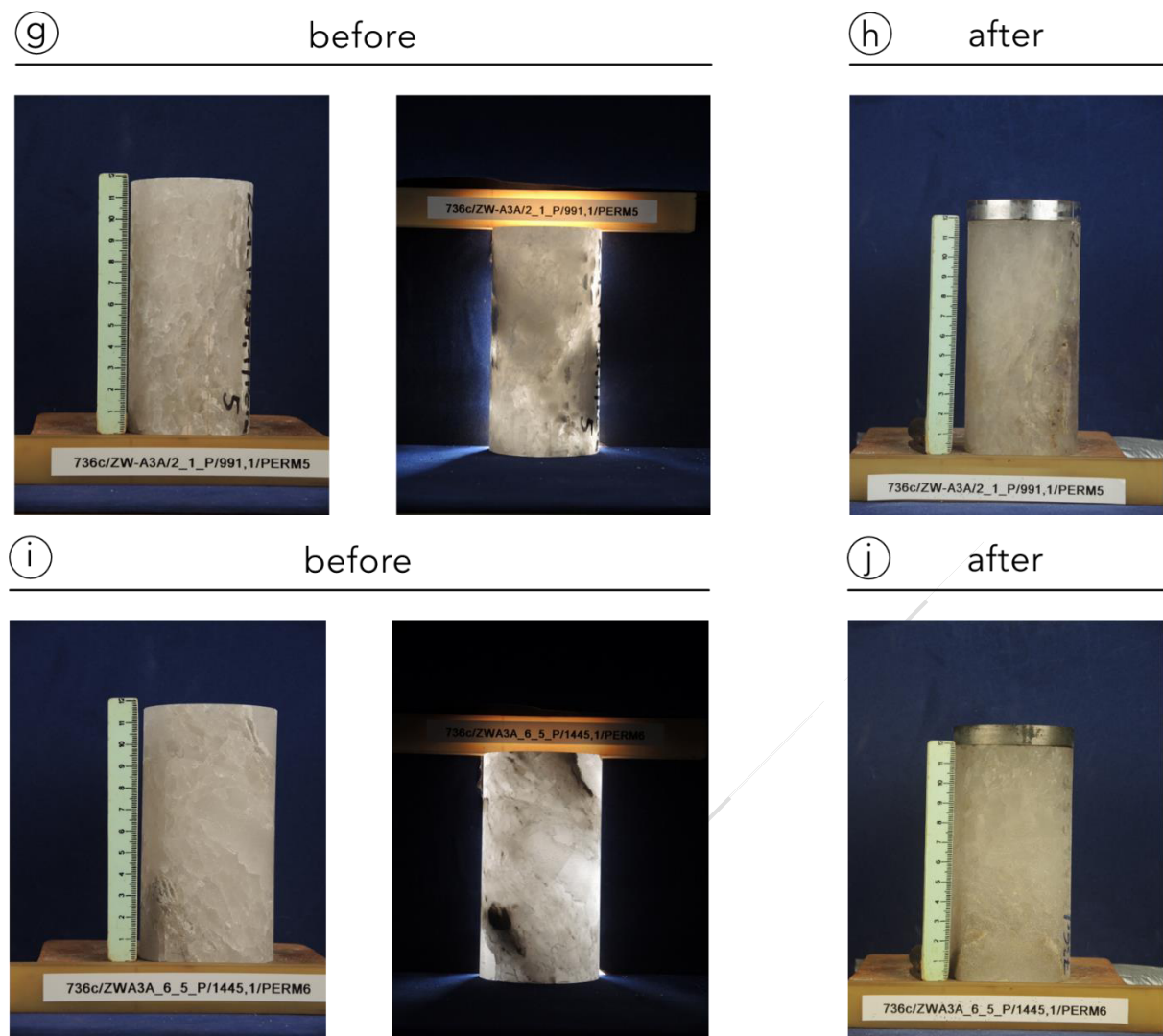


Figure A 11: Specimens prepared to investigate the hydraulic conductivity of the salt material. Subfigures a, c, e, g, i and b, d, f, h, j show samples prior to and after testing, respectively. All experiments have been performed at constant temperature of $T = 40^\circ\text{C}$.

A12: Recorded creep curves and flow paths during hydraulic conductivity testing

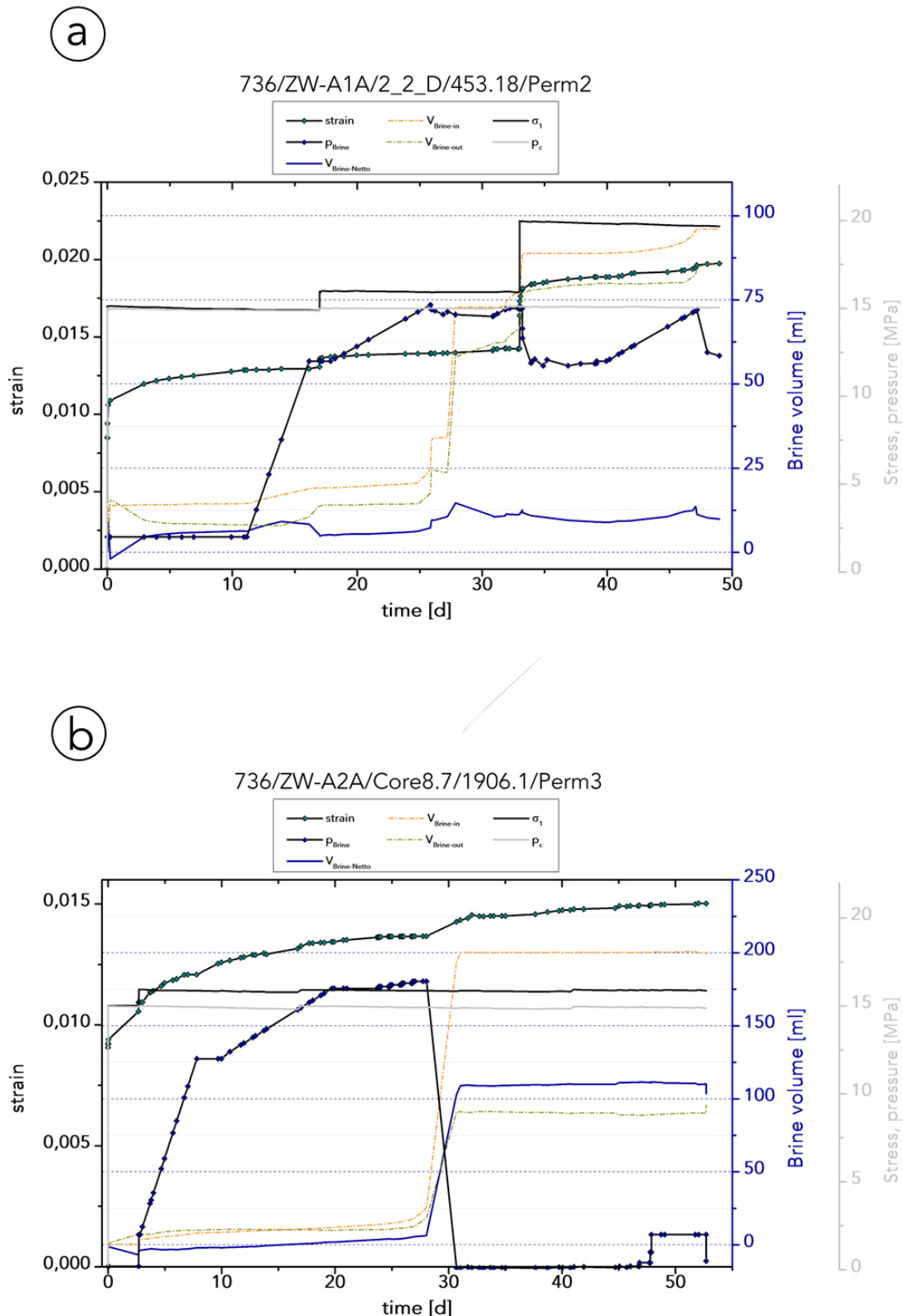
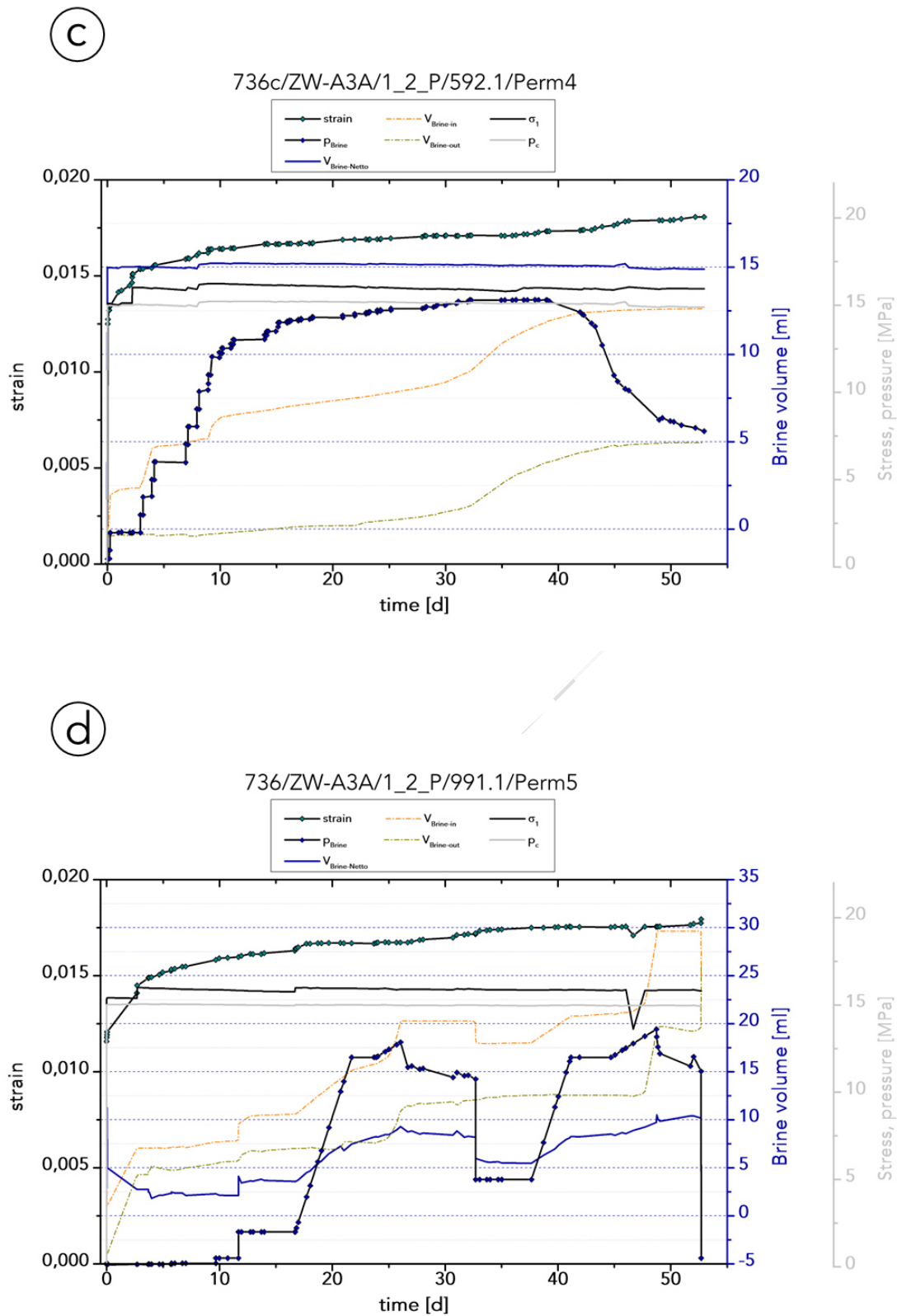
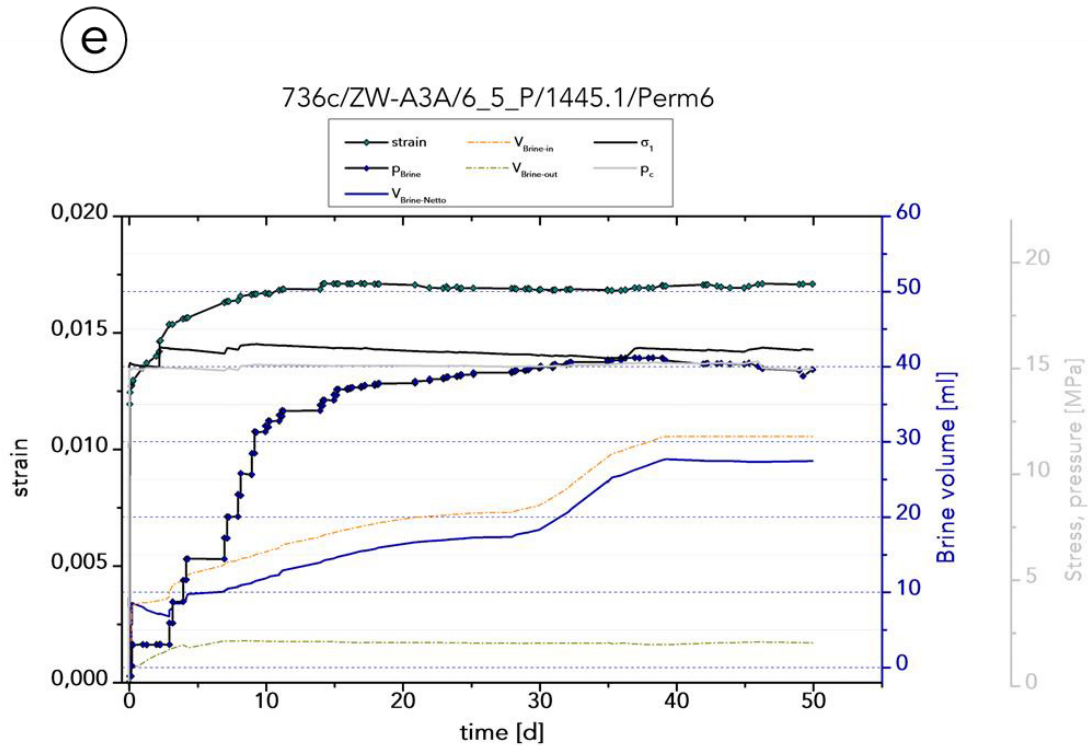


Figure A12: Creep curve including pumped brine volume as well as injection pressure recorded during deformation of samples 736/ZW/Perm2 (a) and 736/ZW/Perm3 (b). During experimental deformation, temperature was held constant at $T = 40^\circ\text{C}$.



Creep curve including pumped brine volume as well as injection pressure recorded during deformation of samples 736/ZW/Perm4 (c) and 736/ZW/Perm5 (d). During experimental deformation, temperature was held constant at $T = 40^\circ\text{C}$.



Creep curve including pumped brine volume as well as injection pressure recorded during deformation of sample 736/ZW/Perm6 (e). During experimental deformation, temperature was held constant at $T = 40^\circ\text{C}$.